Circadian regulation of endoplasmic reticulum calcium response in cultured mouse astrocytes

Ji Eun Ryu[1,2,†], Kyu-Won Shim[3,†], Hyun Woong Roh[1,4,†], Minsung Park[1,2], Jae-Hyung Lee[5*], and Eun Young Kim [1,2*]

[1]Neuroscience Graduate Program, Department of Biomedical Sciences, Ajou University Graduate School of Medicine, Suwon, Kyunggi-do 16499, Republic of Korea

[2]Department of Brain Science, Ajou University School of Medicine, Suwon, 16499, Kyunggi-do, Republic of Korea

[3]Interdisciplinary Program in Bioinformatics, Seoul National University, Seoul 08826, Republic of Korea,

[4]Department of Psychiatry, Ajou University School of Medicine, Suwon, 16499, Kyunggi-do, Republic of Korea

[5]Department of Oral Microbiology, College of Dentistry, Kyung Hee University, Seoul 02447, Republic of Korea

[†]These authors contributed equally.

*Correspondence: ekim@ajou.ac.kr (E.Y.K), Jae-Hyung Lee jaehlee@khu.ac.kr (J.L)

Abstract

The circadian clock, an internal time-keeping system orchestrates 24-hour rhythms in physiology and behavior by regulating rhythmic transcription in cells. Astrocytes, the most abundant glial cells, play crucial roles in central nervous system (CNS) functions, but the impact of the circadian clock on astrocyte functions remains largely unexplored. In this study, we identified 412 circadian rhythmic transcripts in cultured mouse cortical astrocytes through RNA sequencing. Gene Ontology analysis indicated that genes involved in Ca^{2+} homeostasis are under circadian control. Notably, *Herpud1* (*Herp*) exhibited robust circadian rhythmicity at both mRNA and protein levels, a rhythm disrupted in astrocytes lacking the circadian transcription factor, BMAL1. HERP regulated endoplasmic reticulum (ER) Ca^{2+} release by modulating the degradation of inositol 1,4,5-trisphosphate receptors (ITPRs). ATP-stimulated ER Ca^{2+} release varied with the circadian phase, being more pronounced at subjective night phase, likely due to the rhythmic expression of ITPR2. Correspondingly, ATP-stimulated cytosolic Ca^{2+} increases were heightened at the subjective night phase. This rhythmic ER Ca^{2+} response led to circadian phase-dependent variations in the phosphorylation of Connexin 43 (Ser368) and gap junctional communication. Given the role of gap junction channel (GJC) in propagating Ca^{2+} signals, we suggest that this circadian regulation of ER Ca^{2+} responses could affect astrocytic modulation of synaptic activity according to the time of day. Overall, our study enhances the understanding of how the circadian clock influences astrocyte function in the CNS, shedding light on their potential role in daily variations of brain activity and health.

Introduction

The circadian clock orchestrates a range of behaviors, physiological processes, and cellular and biochemical activities in organisms with approximately 24-hour rhythms, facilitating adaptation to environmental changes (Bell-Pedersen et al., 2005). In mammals, the master clock localized in the suprachiasmatic nucleus (SCN) of the anterior hypothalamus synchronizes peripheral tissue clocks throughout the body to the light/dark cycle (Mohawk et al., 2012). The circadian clock's molecular mechanism is driven by a transcriptional translational feedback loop (TTFL). CLOCK and BMAL1 form a heterodimer that triggers expression of the repressor genes, *Period* (*Per*) and *Cryptochrome* (*Cry)*, along with other clock-controlled output genes. PER and CRY proteins then translocate to the nucleus, where they interact with CLOCK/BMAL1, halting further transcriptional activation. A secondary feedback loop involving the interplay between transcriptional activation by ROR and repression by REV-ERB finely regulates the rhythmic transcription of *Bmal1* (Takahashi, 2017). Recent studies have revealed that the circadian clock controls the rhythmic transcription of numerous genes, displaying notable tissue specificity. This characteristic underscores the time-of-day-specific functional specialization of diverse tissues (Mure et al., 2018; Zhang et al., 2014). Consequently, circadian clock-controlled genes significantly influence various physiological processes including development, metabolism, aging, and neurodegeneration (Lananna & Musiek, 2020; Reinke & Asher, 2019; Schultz & Kay, 2003).

Astrocytes, the most abundant glial cells in the CNS, play vital roles in maintaining homeostasis of extracellular fluids, ions, and neurotransmitters; proving energy substrates to neurons; regulating local

blood flow; modulating neuronal activity through gliotransmission; and assisting in interstitial fluid drainage (Sofroniew & Vinters, 2010). Though not electrically excitable, astrocytes exhibit complex intracellular Ca^{2+} signaling, both spatially and temporally, within individual astrocytes and across astrocytic networks. Astrocytes express various types of Gq-coupled receptors activated by neurotransmitters such as ATP, epinephrine, glutamate, and dopamine *etc*. (Verkhratsky & Nedergaard, 2018). Activation of these Gq-coupled receptors initiates the inositol 1,4,5-trisphosphate receptor (IP_3R) signaling cascade, causing a release of Ca^{2+} from the ER that substantially increases intracellular Ca^{2+} levels (Guerra-Gomes et al., 2017; Verkhratsky & Nedergaard, 2018). Increases in intracellular Ca^{2+} in astrocytes are involved in regulating numerous afore-mentioned processes (Giaume et al., 2021; Verkhratsky & Nedergaard, 2018). Recent studies have shown that astrocyte Ca^{2+} signaling can regulate circadian rhythms and sleep patterns (Bojarskaite et al., 2020; Brancaccio et al., 2019).

Accumulating evidence underscores the importance of the circadian clock in astrocytes function. Cultured murine cortical astrocytes expressing a PER-luciferase reporter (PER::LUC) exhibit circadian oscillations and can be entrained by temperature cycle (Prolo et al., 2005) and vasoactive intestinal polypeptide (VIP), which synchronizes SCN (Marpegan et al., 2009). These findings provide strong evidence that a molecular clock operates in astrocytes. In addition, disruption of clock genes specific to astrocytes has been linked to a range of deleterious effects, including excessive astrocyte activation, disruptions in daily activity patterns, impaired learning, metabolic imbalances, and a shortened lifespan (Barca-Mayo et al., 2020; Barca-Mayo et al., 2017; Griffin et al., 2019; Lananna et al., 2018). Remarkably, these phenotypic changes closely resemble those observed in astrocytes during the progression of neurodegenerative diseases (Brandebura et al., 2023; Phatnani & Maniatis, 2015). Moreover, the rhythmic metabolic activity of astrocytes, including intracellular Ca^{2+} fluctuations and neurotransmitter release, is critical for circadian timing in the SCN (Brancaccio et al., 2017). Despite the emerging significance of circadian rhythms in astrocyte function in health and disease, our understanding of the link between the circadian clock and specific astrocytic functions is still limited.

In this study, we conducted a transcriptome analysis to investigate how the circadian clock regulates astrocyte function. Our research uncovered that *Herp (*homocysteine-inducible ER protein with ubiquitin like domain 1; *Herp*) exhibited a BMAL1-dependent rhythmic expression, peaking at subjective midday phase and reaching its nadir at subjective midnight phase. HERP was crucial for ER Ca^{2+} regulation by modulating the degradation of ITPRs. Importantly, the ATP-stimulated ER Ca^{2+} response varied according to time post synchronization, a dependence that was absent in cultured astrocytes from *Bmal1*$^{-/-}$ mice. Furthermore, the pronounced release of Ca^{2+} during the subjective night phase led to robust phosphorylation of the Ser368 residue of CX43, diminishing cell-to-cell communication between astrocytes. Overall, our study demonstrates that the circadian clock orchestrates a variety of astrocytic processes including Ca^{2+} homeostasis by controlling the rhythmic transcription of genes, highlighting its pivotal role in CNS function.

Results

Defining circadian rhythmic transcripts in cultured mouse cortical astrocytes

To understand how the circadian clock regulates astrocyte physiology, we conducted a circadian transcriptome analysis of cultured mouse cortical astrocytes. Cultured astrocytes were synchronized using serum shock (SS) and harvested every 4hrs for 2 days starting at 12hrs post-SS. The time series astrocyte transcriptome was determined by RNA-seq (Figure 1A). Using a Gaussian mixture model, we defined expressed transcripts, choosing 0.577 transcripts per million (TPM) as the cut-off, corresponding to the 1% threshold in the distribution curve of highly expressed genes (Figure 1-figure supplement 1A). A total of 17,671 transcripts with the highest TPM values of the 12 time points exceeding 0.577, were considered expressed. To validate astrocyte enrichment, we compared the expression of marker genes for nervous cells. Our transcriptome data were replete with astrocyte markers but lacked markers for microglia, oligodendrocytes, neurons, and endothelial cells (Figure 1-figure supplement 1B).

Various methods have been used to identify periodicity in time-series data, such as Lomb-Scargle (Glynn et al., 2006), JTK_CYCLE (Hughes et al., 2010) and ARSER (Yang & Su, 2010), each with distinct advantages and limitations. MetaCycle, integrates these three methods, facilitating the evaluation of periodicity in time-series data without requiring the selection of an optimal algorithm (Wu et al., 2016). Additionally, BioCycle has been developed using a deep neural network trained with extensive synthetic and biological time series datasets (Agostinelli et al., 2016). Because MetaCycle and Biocycle identify periodic signal based on different algorithms, we applied both packages to identify periodicity in our time-

series transcriptome data. BioCycle and MetaCycle analyses detected 321 and 311 periodic transcripts, respectively (FDR corrected, q-value < 0.05) (Figure 1B). Among these, 220 (53.4%) were detected by both methods, but many transcripts did not overlap. MetaCycle is known for its inability to detect asymmetric waveforms (Mei et al., 2020). In our analysis, genes with increasing waveforms like *Adora1* and *Mybph* were identified as rhythmic only by BioCycle, while *Plat* and *Il34* were identified as rhythmic only by MetaCycle (Figure 1-figure supplement 1C). Despite these discrepancies, the clear circadian rhythmic expression profiles of these genes led us to conclude that using the union of the two lists compensates for the limitations of each algorithm. Consequently, we identified a total of 412 circadian rhythmic transcripts (2.3% of all transcripts) (Supplementary file 1). The circadian oscillations of these transcripts are illustrated in the heatmap in Figure 1-figure supplement 1D.

Next, we compared rhythmic transcripts of astrocytes with those of 12 mouse tissues from CircaDB (Zhang et al., 2014), a database of circadian rhythmic genes (Figure 1C). A majority of the rhythmic transcripts in astrocytes (265 of 412, 65.3%) were not rhythmic or were rhythmic in one tissue. 14 transcripts were rhythmic in more than 10 tissues; most of these were core clock genes except *Tspan4*, *Tsc22d3*, and *Wee1*. This result is consistent with previous reports of tissue-specific circadian rhythmic expression (Mure et al., 2018; Panda et al., 2002). A phase comparison of these 14 common oscillating transcripts between CircaDB and our analysis showed a consistent time difference, with 8hrs after SS corresponding to ZT0 (Figure 1D). An additional phase comparison of 82 transcripts that overlapped in only one tissue indicated a very robust phase correlation between astrocytes and the corresponding tissue (r = 0.69, p < 0.001) (Figure 1E). Collectively, our analysis indicates that the identified oscillating transcripts were not false positive but were clearly associated with the circadian clock. Hierarchical clustering analysis of oscillating transcripts revealed two clusters: cluster 1 with 185 transcripts and cluster 2 with 227 transcripts (Figure 1-figure supplement 2). A circular map of peak phases across all rhythmic genes revealed two major peaks, one in the early night (ZT12 to ZT16) and one in the late night or dawn (ZT21 to ZT1) (Figure 1F). Here for more intuitive interpretation, we set 8hrs post synchronization (sync) to ZT0 based on a previous phase comparison. Circadian transcriptome studies conducted in multiple animal tissues have indicated that the phases of each tissue are not randomly distributed but are predominantly clustered in one or two narrow temporal windows (Panda et al., 2002). Consistent with these previous reports, mouse cultured astrocytes exhibited a high degree of temporal organization. Intriguingly, there was a relatively quiescent zone during subjective daytime, a finding different from that observed for diurnal animals, which showed a quiescent zone during subjective nighttime (Mure et al., 2018).

To understand the biological processes and pathways controlled by the circadian clock, we performed a Gene Ontology (GO) analysis on each cluster using Metascape (https://metascape.org) (Figure 1G). Given that the goal of our research was to investigate processes specifically controlled by the circadian clock, we excluded 17 core clock transcripts (*Arntl, Clock, Nfil3, Npas2, Bhlhe40, Bhlhe41, Cry1, Cry2, Dbp, Elf, Nr1d1, Nr1d2, Per1, Per2, Per3, Rorc,* and *Tef*) from our GO enrichment analysis. Among the rhythmic processes, we focused on "calcium ion homeostasis (GO:0055074)" due to the importance of intracellular Ca^{2+} signaling in numerous astrocyte functions (Agulhon et al., 2008; Bojarskaite et al., 2020; Brancaccio et al., 2019; Giaume et al., 2021; Guerra-Gomes et al., 2017; Verkhratsky & Nedergaard, 2018). In this category, Ca^{2+} homeostasis-related genes included *Herp*, *Slc4a11*, *Sord* and *Kcnh1 etc*. with *Herp* showing the most robust oscillation with large amplitude (Table S1).

Circadian rhythmic expression of *Herp* in cultured mouse cortical astrocytes

We first assessed the expression patterns of core clock genes and *Herp* in our cultured astrocytes. *Bmal1*, was rhythmically expressed with a peak at 30hr post sync while *Per2* and *Rev-Erb*α showed rhythmic expression with peaks at 20hr and 16hr, respectively (Figure 2A). *Herp* displayed a robust rhythmic expression pattern, peaking at 20hr, similar to *Per2* (Figure 2A). To verify the circadian expression of *Herp*, we performed quantitative real-time RT-PCR, which confirmed that *Bmal1*, *Rev-Erb*α and *Herp* exhibited circadian rhythms consistent with the RNAseq results (Figure 2B).

Next, we examined whether HERP protein levels also showed rhythmic changes, as many genes exhibit rhythmic transcription without corresponding protein level changes (Reddy et al., 2006). We validated the specificity of HERP antiserum using Western blot analysis of astrocytes treated with *Herp* siRNA (*Herp*-KD), which significantly reduced *Herp* mRNA levels (Figure 2C) and the intensities of specific bands in Western blots (Figure 2D and 2E). SS-synchronized cultured astrocytes were sampled every 6hrs for 2 days and processed for Western blot analysis of BMAL1 and HERP. BMAL1 phosphorylation showed circadian variation, with hyper-phosphorylation peaking at midday and hypo-phosphorylation peaking early

in the day or late at night (Yoshitane et al., 2009). In our SS-synchronized cultured astrocytes, BMAL1 was hyperphosphorylated at 18hr, 24hr, 42hr, and 48hr (corresponding to midday) and hypo-phosphorylated at 12hr, 36hr (corresponding to early in the day), and 30hr, 54hr (corresponding to late at night) throughout two daily cycles (Figure 2F) indicating strong circadian rhythms in cultured astrocytes. Importantly, HERP protein levels oscillated peaking at 18hr and 42hr and reaching a minimum at 12hr, 30hr, and 54hr, mirroring its mRNA pattern (Figure 2F and 2G).

Herp also exhibited rhythmic expression in astrocyte cultures synchronized by either dexamethasone (Balsalobre et al., 2000) or forskolin (Yagita & Okamura, 2000) treatments which are other commonly used for circadian clock resetting (Figure 2-figure supplement 1). Finally, to investigate whether the rhythmic expression of *Herp* is regulated by a circadian clock, we examined *Herp* mRNA and protein expression patterns in primary astrocyte cultured from *Bmal1*$^{-/-}$ mice. The rhythmic expression patterns of *Per2*, *Rev-Erbα*, and *Herp* were abolished in *Bmal1*$^{-/-}$ astrocyte cultures with their expression maintained at trough levels (Figure 2A). HERP protein levels remained constant throughout the daily cycles (Figure 2H and 2I). Collectively, these observations indicate that the expression of *Herp* exhibits a robust circadian rhythm that is controlled by BMAL1 in cultured mouse astrocytes. These results suggest that HERP-regulated cellular processes vary in a time-of-day specific manner.

Herp knockdown alters ATP-induced ER Ca^{2+} release

Herp was first identified as a gene with altered expression in response to homocysteine treatment in human umbilical vein endothelial cells (HUVECs) (Kokame et al., 1996). It is strongly induced not only by homocysteine but also by ER stress-causing agents such as tunicamycin or thapsigargin. HERP, characterized by an N-terminal ubiquitin-like domain and present in the ER membrane facing cytoplasmic side, is involved in the unfolded protein response (UPR) (Kokame et al., 2000) and is part of the ER-associated degradation (ERAD) complex, participating in the ubiquitination and relocation of ERAD substrates (Leitman et al., 2014). Notably, HERP modulates the ER Ca^{2+} response through IP_3R degradation (Paredes et al., 2016; Torrealba et al., 2017).

Thus, we sought to investigate whether HERP-controlled processes are subject to circadian regulation by examining the HERP-regulated ER Ca^{2+} response in the astrocytes. We employed the organelle-specific fluorescent Ca^{2+} indicators: G-CEPIA1er for the ER (Suzuki et al., 2014), R-GECO1 for the cytosol (Wu et al., 2013), and mito-R-GECO1 for mitochondria (Zhao et al., 2011). We first confirmed that these Ca^{2+} indicators colocalized with organelle-specific markers (Figure 3-figure supplement 1). ATP serves not only as a fundamental energy source but also as an active intercellular messenger. In astrocytes, ATP application induces an increase in intracellular Ca^{2+} (Neary et al., 1988) by binding to the G_q/G_{11} coupled P2Y receptor, activating PLC-β and inducing the hydrolysis of PIP_2 to diacylglycerol (DAG) and IP_3, which mobilizes Ca^{2+} through IP_3Rs on the ER membrane (Baryshnikov et al., 2003; James & Butt, 2001).

We treated control and *Herp*-KD astrocytes with 100μM ATP and monitored subcellular Ca^{2+} changes. ATP treatment rapidly decreased ER Ca^{2+} in control astrocytes and this response was more pronounced in *Herp*-KD astrocytes (Figure 3A-3C). As the main Ca^{2+} store in the cell, ER releases Ca^{2+} which is then rapidly transmitted to other organelles such as mitochondria and cytosol (Carreras-Sureda et al., 2018; Giorgi et al., 2018). Although ATP treatment did not significantly alter cytosolic Ca^{2+} signal in control astrocytes, it greatly increased cytosolic Ca^{2+} signals in *Herp*-KD astrocytes (Figure 3D-3F). Consistently, mitochondrial Ca^{2+} significantly increased in *Herp*-KD astrocytes compared with control (Figure 3G-3I).

Next, we examined the mechanism by which HERP controls ER Ca^{2+}.There are three subtypes of IP_3Rs encoded by the genes *Itpr1*, *Itpr2*, and *Itpr3*. Transcriptome analysis of our cultured astrocytes indicated *Itpr1* as the most prevalent, followed by *Itpr2*, while *Itpr3* expression was minimal (Figure 3-figure supplement 2). Notably, expression of these *Itpr* subtypes was not rhythmic. We then assessed the ITPR1 and ITPR2 protein levels in control and *Herp*-KD astrocytes and found that the levels of both ITPR1 and ITPR2 were slightly but statistically significantly increased in *Herp*-KD astrocytes compared to controls (Figure 3J-3M). These results, consistent with previous reports (Paredes et al., 2016; Torrealba et al., 2017) indicated that HERP negatively regulates ITPRs in astrocyte.

To confirm that the HERP-ITPR axis underlies ER Ca^{2+} response, we analyzed the ER Ca^{2+} response following treatment with Xestospongin C (XesC), an IP3R inhibitor. XesC treatment reduced the ATP-induced ER Ca^{2+} release and abolished the enhanced effect observed in *Herp*-KD compared to control (Figure 3N-3P). Collectively, these results clearly indicate that HERP controls ER Ca^{2+} release by negatively regulating IP3Rs.

ATP-induced ER Ca^{2+} release varies according to time post synchronization

Given that HERP levels exhibited circadian variation and HERP regulated ER Ca^{2+} release, we investigated whether ATP-induced ER Ca^{2+} responses differ depending on circadian phase. After SS, we measured ER Ca^{2+} following ATP treatment at peak (42hr post sync) and trough (30hr post sync) phases of HERP (Figure 4A). With lower HERP levels potentially resulting in higher IP_3R levels at 30hr, we anticipated greater ER Ca^{2+} release at 30hr than at 42hr. Consistent with this, ER Ca^{2+} decreased more at 30hr than at 42hr upon ATP treatment (Figure 4B-4D). Also, in keeping with previous result (Figure 3A-3I), cytosolic Ca^{2+} increased more at 30hr than at 42hr following ATP treatment (Figure 4E-4G). Although mitochondrial Ca^{2+} responses exhibited a similar trend, the differences were not statistically significant (Figure 4H-4J).

To confirm that HERP underlies this circadian phase-dependent ER Ca^{2+} release, we compared ER Ca^{2+} release in control and *Herp*-KD astrocytes at 30hr and 42hr post sync. Control astrocytes exhibited time-dependent variation in ER Ca^{2+} release, which was abolished in *Herp*-KD astrocytes (Figure 4K-4L), indicating the involvement of HERP in this regulation.

We then assessed whether ITPR1 and ITPR2 levels varied with time. BMAL1 phosphorylation served as a proxy for circadian phase (Figure 4N). ITPR2 levels showed time-dependent changes opposite to those of HERP, whereas ITPR1 levels remained constant (Figure 4N and 4O). Since *Itpr2* mRNA levels did not exhibit a rhythmic pattern (Figure 3-figure supplement 1), the circadian phase-dependent differences in ITPR2 levels are likely driven by HERP-mediated ITPR2 degradation. Consequently, circadian rhythmic ER Ca^{2+} release is primarily driven by oscillations in ITPR2.

To verify if ER Ca^{2+} release is regulated by the circadian clock, we analyzed the ER Ca^{2+} response in *Bmal1*$^{-/-}$ mouse astrocyte cultures. In WT astrocyte cultures, there was a clear circadian phase-dependent difference in ER Ca^{2+} release. However, this difference was abolished in *Bmal1*$^{-/-}$ astrocyte cultures (Figure 5A-C). The absence of rhythmic ER Ca^{2+} release in *Bmal1*$^{-/-}$ astrocytes correlated with constant levels of HERP (Figure 5D-E). Additionally, ER Ca^{2+} release was significantly faster in *Bmal1*$^{-/-}$ astrocytes compared to WT astrocytes (Figure 5A-C) attributed to lower levels of HERP in *Bmal1*$^{-/-}$ astrocytes (Figure 5D-E). Collectively, these results indicate that ER Ca^{2+} release is regulated by HERP, which is under circadian clock control.

ATP-induced S368-phosphorylation of CX43 and gap junctional communication shows circadian variation.

Syncytial coupling through gap junctions is a prominent feature of astrocytes, critical for their homeostatic functions, including the diffusion and equilibration of ions, metabolites, and signaling molecules (Langer et al., 2012; Verkhratsky & Nedergaard, 2018). This coupling allows the astrocytic syncytium to propagate Ca^{2+} waves, affecting nearby and remote cells through release of “gliotransmitters” and modulating synaptic functions in a far-reaching network (Pacholko et al., 2020). Connexin (Cx) family proteins constitute gap junction channels (GJCs) (Giaume et al., 2021), with Cx43 (also known as Gja1) and Cx30 (also known as Gjb6) being the main connexins in astrocytes (Kunzelmann et al., 1999; Nagy et al., 1999). In our cultured astrocytes, Cx43 was the most abundantly expressed connexin (Figure 6-figure supplement 1). Phosphorylation of CX43 at Ser368 by protein kinase C (PKC), activated in response to intracellular Ca^{2+}, is known to decrease gap junction conductance (Enkvist & McCarthy, 1992; Nimlamool et al., 2015; Solan & Lampe, 2014). Accordingly, we hypothesized that the circadian variations in ATP-driven ER Ca^{2+} responses might differentially impact CX43 phosphorylation according to times of day.

First, we confirmed that ATP treatment induces rapid phosphorylation of CX43 at Ser368 (pCX43 (S368)) in cultured astrocytes (Figure 6A and 6B). We then examined whether pCX43 (S368) varies with circadian phase. Notably, ATP-induced ER Ca^{2+} release was more pronounced at 30hr than at 42hr post sync (Figure 3), and pCX43 (S368) in response to ATP was also significantly higher at 30hr compared to 42hr post sync (Figure 6C and 6D).

We also examined circadian variations of pCX43 (S368) *in vivo*. Mice were entrained to a 12:12 hour light/dark (LD) cycle for two weeks and then kept in constant darkness (DD). This ensured that variations in CX43 phosphorylation were due to the internal circadian clock and not external light stimuli. Prefrontal cortex tissues were dissected at circadian time (CT) 58 and CT70 on the third day of DD. pCX43 (S368) levels were higher at CT70 (subjective night) than at CT58 (subjective day), consistent with our *in vitro* results (Figure 6E and 6F).

To confirm that HERP underlies the rhythmic phosphorylation of CX43 at Ser368, we compared pCX43 (S368) in control and *Herp*-KD astrocytes at 30hr and 42hr post sync. In control astrocytes pCX43 (S368)

was higher at 30hr compared to 42hr, consistent with previous results. However, in *Herp*-KD astrocytes, the circadian phase-dependent differences in pCX43 (S368) were abolished despite the normal circadian rhythm indicated by BMAL1 phosphorylation, (Figure 6G and 6H). This suggests that rhythms of HERP levels are required for the rhythmic phosphorylation of CX43 (S368).

Finally, we assessed if rhythmic phosphorylation of CX43 contributes to circadian phase-dependent variation in gap junctional communication in cultured astrocytes by using fluorescence recovery after photobleaching (FRAP) method. The absence of FRAP signal in carbenoxolone (CBX)-treated astrocytes confirmed the involvement of gap junctions in intercellular communication of cultured astrocytes (Figure 7A-7C). We observed a faster and more pronounced recovery of fluorescence in photobleached astrocytes at 42hr compared to 30hr post sync (Figure 7D-7F). Importantly, this variation was absent in astrocytes cultured from *Bmal1*$^{-/-}$ mice, indicating that circadian clock regulates gap junctional communication (Figure 7G.-7I).

In summary, we propose a model illustrating how the circadian clock influences astrocyte function through the regulation of ER Ca^{2+} response. Based on phase comparisons of clock genes between our data and CircaDB (Figure 1D), we defined subjective day and night, with 8hr post sync corresponding to the beginning of the day. In astrocytes, BMAL1/CLOCK-controlled oscillation of HERP regulates day and night variations in ITPR2 levels. These oscillations contribute to changes in ER Ca^{2+} responses, which in turn result in the distinct day and night differences in pCx43 (S368) and the gap junction conductance (Figure 7J).

Discussion

It is widely acknowledged that the circadian clock orchestrates cellular functions in a highly cell type-specific manner by governing transcription (Mure et al., 2018; Zhang et al., 2014). Although the importance of the circadian clock in astrocytes has been well-documented (Barca-Mayo et al., 2020; Barca-Mayo et al., 2017; Griffin et al., 2019; Lananna et al., 2018; Prolo et al., 2005; Tso et al., 2017), studies specifically exploring astrocyte-specific circadian transcriptomes have been limited. Our study conducted such an analysis on primary cultured cortical astrocytes, discovering that rhythmic expression of *Herp* underlies day/night variation in ER Ca^{2+} response by regulating IP_3R levels. We also found that Ca^{2+}-activated CX43 phosphorylation varied according to the daily rhythmic ER Ca^{2+} response. Given that astrocytes function in a network in which Ca^{2+} propagates through GJCs, we propose that the time-dependent control of ER Ca^{2+} responses could influence the role of astrocytes in modulating synaptic activity throughout the day (see below).

Circadian oscillations of *Herp* expression have been previously documented in various mouse tissues including the lung, heart, liver, kidney, aorta, skeletal muscle, adrenal gland, pancreatic islet and SCN (Panda et al., 2002; Rakshit et al., 2016; Zhang et al., 2014). In this study, we identified that *Herp* is also rhythmically expressed in cultured astrocytes. *Herp* exhibited rhythmic expression in phase with *Per2* and showed flattened expression at its nadir level in *Bmal1*$^{-/-}$ astrocyte cultures, suggesting direct regulation CLOCK/BMAL1 heterodimers (Figure 2A). ChIP-Atlas analysis (https://chip-atlas.org) (Oki et al., 2018; Zou et al., 2022) has shown CLOCK binding to the genomic region of *Herp* (Annayev et al., 2014; Hong et al., 2018). Although no canonical E-Box is present in the upstream 6kb region of the *Herp* gene, several non-canonical E-Boxes, important for circadian expression (Yoo et al., 2005; Zhang et al., 2011), were identified (Table S2). Among these, the non-canonical E-Box sequence “CACGTT,” located near transcription start site (chr8:94386194-94386543), is highly conserved across diverse mammalian species. Therefore, we propose that these non-canonical E boxes might drive the CLOCK/BMAL1 dependent expression of *Herp*.

A recent study employing a circadian single-cell RNA seq analysis of SCN reported that *Herp* displays a circadian rhythm exclusively in astrocytes and oligodendrocytes (Wen et al., 2020). Given that astrocytic Ca^{2+} levels in the SCN show a circadian rhythm, peaking during the subjective night and are crucial for circadian timing (Brancaccio et al., 2019; Patton et al., 2022), HERP’s circadian rhythmic expression in SCN astrocytes (Wen et al., 2020) may be integral to the mechanisms of circadian timing.

We demonstrated that HERP regulated ER Ca^{2+} responses by degrading IP_3Rs in astrocytes (Figure 3J-3M). (Paredes et al., 2016; Torrealba et al., 2017). When *Herp* was downregulated, both ITPR1 and ITPR2 levels increased, suggesting HERP’s role in degrading both ITPR1 and ITPR2. However, only the levels of ITPR2 exhibited circadian phase-dependent variation (Figure 3J-3M, Figure 4K-4L). The min/max ratio of HERP expression throughout the day was 0.38 under normal conditions but 0.072 in *Herp*-KD conditions. Based on this, we reasoned that the amplitude of HERP oscillations impacted the levels of ITPR2 under

normal circumstances, while having a much lesser effect on the levels of ITPR1. Thus, the circadian control of ER Ca^{2+} release in response to stimulation in cultured astrocytes is primarily attributable to ITPR2.

ER and cytosolic Ca^{2+} responses following ATP treatment exhibited distinct circadian variation, but mitochondrial Ca^{2+} responses did not show significant variations (Figure 4). We think of several possibilities to account for the absence of significant circadian variations in mitochondrial Ca^{2+} relative to cytoplasmic Ca^{2+} change. Upon ATP stimulation, direct Ca^{2+} transfer occurs through IP_3R in the cytosol. For mitochondrial uptake, Ca^{2+} first transits to the intermembrane space via IP_3Rs and the voltage-dependent anion channel (VDAC) complex before entering the matrix through mitochondrial calcium uniporter (MCU) (Giorgi et al., 2018). The Mito-R-GECO1 reporter is confined within the mitochondrial matrix and thus limiting assessment of Ca^{2+} levels in the intermembrane space (Wu et al., 2013). Substantial changes in Ca^{2+} levels might occur in the intermembrane space, but the influx into the matrix via MCUs could remain constant across different time, resulting in apparent lack of significant change. Secondly, the amount of VDAC or the VDAC:IP_3R complex on the mitochondrial membrane might vary inversely with HERP levels, potentially maintaining a consistent flow of Ca^{2+} into the mitochondria irrespective of the time. Additionally, the presence of several Ca^{2+} extrusion mechanisms in mitochondria (Giorgi et al., 2018) points to a more complex regulation of Ca^{2+} compared with that in the cytosol. Although the precise mechanism remains to be elucidated, our data indicate that the circadian variation in Ca^{2+} release from the ER, particularly in response to stimuli, predominantly impacts cytoplasmic signaling rather than mitochondrial signaling.

During the subjective night phase (active period for mice), ATP- stimulated ER Ca^{2+} release was pronounced than during the subjective day phase (rest period for mice) (Figure 4). This finding aligns with studies showing heightened stimulus-evoked Ca^{2+} activity in astrocytes during wakefulness, which diminishes during sleep (Bojarskaite et al., 2020; Ingiosi et al., 2020). In flies, Ca^{2+} activity in astrocytes is correlated with the duration of wakefulness, suggesting that astrocytic Ca^{2+} is a key factor in the homeostatic regulation of sleep (Blum et al., 2021). Our findings provide a mechanistic explanation for differential Ca^{2+} levels observed between wake and sleep states, with circadian regulation of ITPR2 by HERP being a key factor in this process.

ATP-stimulated Cx43 (S368) phosphorylation is higher at 30hr (subjective night phase) than at 42hr post sync (subjective day phase) (Figure 6C and 6D.), a finding further supported by in *vivo* experiments (Figure 6E and 6F). What are the implications of this day/night variation in CX43 (S368) phosphorylation? We reasoned that the circadian variation in CX43 phosphorylation could significantly impact astrocyte functionality within the syncytium. Indeed, our cultured astrocytes exhibited circadian phase-dependent variation in gap junctional communication (Figure7D-7F). Astrocytes influence synaptic activity through the release of gliotransmitters such as glutamate, GABA, D-serine, and ATP, triggered by increases in intracellular Ca^{2+} in response to the activity of adjacent neurons and astrocytes (Verkhratsky & Nedergaard, 2018). Importantly, this increase in Ca^{2+} spreads to adjacent astrocytes through GJCs (Fujii et al., 2017), influencing a large area of the neuronal network. Considering that Cx43 Ser368 phosphorylation occurs to uncouple specific pathways in the astrocytic syncytium to focus local responses (Enkvist & McCarthy, 1992), our findings suggest that astrocytes better equipped for localized responses when presented with a stimulus during the active phase in mice. Conversely, during the rest period, characterized by more synchronous neuronal activity across broad brain areas (Vyazovskiy et al., 2009) higher GJC conductance might allow astrocytes to exert control over a larger area. In support of this idea, recent study showed that synchronized astrocytic Ca^{2+} activity advances the slow wave activity (SWA) of the brain, a key feature of non-REM sleep (Szabó et al., 2017). Blocking GJC was found to reduce SWA, further supporting this interpretation. However, conflicting findings have also been reported. For instance, Ingiosi et al. (Ingiosi et al., 2020) found that astrocytic synchrony was higher during wakefulness than sleep in the mouse frontal cortex. Whether these differing results in astrocyte synchrony during resting and active periods are attributable to differences in experimental context (e.g., brain regions, sleep-inducing condition) remains unclear. Indeed, astrocyte Ca^{2+} dynamics during wakefulness/sleep vary according to brain regions (Tsunematsu et al., 2021). While the extent of astrocyte synchrony might differ depending on brain region and/or stimulus, our results suggest that the baseline state of astrocyte synchrony, which is affected by GJC conductance, varies with the day/night cycle.

In conclusion, our findings enhance the understanding of the circadian regulation of astrocytic functions, particularly through the rhythmic expression of HERP and its impact on ER Ca^{2+} signaling and CX43 phosphorylation. This study underscores the intricate interplay between the circadian clock and astrocyte physiology, highlighting the pivotal role of HERP in modulating key astrocytic processes such as sleep, gap junction communication and synaptic modulation. The day/night variations in ER Ca^{2+} response and CX43

390 phosphorylation, and their implications for astrocytic network dynamics and neuronal interactions, open
391 new avenues for exploring the broader implications of astrocytic circadian rhythms in brain function and
392 health.
393
394 **Materials and Methods**
395 **Animals**
396 All procedures for the care and use of laboratory animals were approved by the Institutional Animal Care
397 and Use Committee (IACUC) of Ajou University School of medicine. *Bmal1*$^{-/+}$ mice (B6.129-Bmal1^{tm1Bra}/J;
398 Jackson Laboratory, #009100)(Bunger et al., 2000) were purchased from Jackson Laboratory(USA) and
399 housed in a specific pathogen-free environment at the Animal Research Center of Ajou University Medical
400 Center, with a standard 12-hour light/dark cycle and free access to food. Primary cultured astrocytes
401 involving only WT mice used 1day-old C57BL/6 mice (Koatch Inc., Korea). In experiments employing
402 primary cultured astrocytes from *Bmal1*$^{-/-}$ mice, wild type (WT) littermates were used as controls. For
403 animal studies, 7-8 week-old adult C57BL/6 male mice were first entrained in a standard 12-hour light/dark
404 cycle for 2 weeks and then maintained in a constant darkness (DD). On the third day of DD, mice were
405 sacrificed at indicated time and its prefrontal cortex (PFC) was dissected.
406
407 **Primary astrocyte culture**
408 Primary astrocyte culture was prepared according to a previous report (Choi et al., 2018) with minor
409 modifications. In brief, 1 day old pups were anesthetized by hypothermia and their cerebral cortices were
410 dissected out and triturated in Modified Eagle's medium (MEM; Welgene, Korea, LM 007-11) containing
411 10% fetal bovine serum (FBS; Hyclone, USA, SV30207.02), penicillin/streptomycin (Gibco, USA, 15140-
412 122), 10 μM HEPES (Gibco, USA, 15630080) and GlutaMAX (Gibco, USA, 35050-061) yielding a single-
413 cell suspension. Cells were plated into 75 cm^2 T-flasks (1pup/flask) and incubated at 37°C in a humidified
414 5% CO_2 incubator for 2 weeks. Primary astrocytes were then incubated in a serum-free MEM for 7 days,
415 after which astrocytes were detached from the T-flask with 0.25% trypsin and plated on culture dishes
416 ($1.0X10^6$cells/60 mm dish) for experiments.
417
418 **Circadian transcriptome analysis**
419 The experimental scheme for synchronizing circadian clocks of cultured astrocyte is illustrated in Figure 1A.
420 In brief, astrocytes were grown in dishes ($1.0 X 10^6$cells/60 mm dish) until reaching complete confluence
421 and then incubated in serum-free MEM for 72hrs. Cells were then subjected to serum shock (SS), a well-
422 established procedure for synchronizing the circadian clock of cultured cells (Balsalobre et al., 1998), by
423 exchanging the medium for MEM containing 50% horse serum. 12hrs post SS, astrocytes were harvested
424 at 4-h intervals for 2 days for RNA sequencing (RNA-seq). Total RNA was extracted and purified from
425 harvested astrocytes using a RNeasy Plus Micro Kit (Qiagen, Germany, 74034). RNA quality and quantity
426 assessments, RNA-Seq library construction, and next-generation sequencing analysis were performed by
427 Macrogen Inc. (Korea). Total RNA integrity and library size were analyzed using an Agilent Technologies
428 2100 Bioanalyzer. Paired-end raw reads, generated using an Illumina HiSeq 2000 system, were aligned to
429 the mm10 mouse genome using STAR aligner (v.2.5.2b)(Dobin et al., 2013). Gene expression was
430 subsequently quantified by calculating transcripts per million (TPM) using Ensemble gene (release 82)
431 annotations. The threshold for defining expressed transcripts was set using a Gaussian mixture model in
432 the R package 'mixtools'. To detect circadian oscillating transcripts, we employed two circadian oscillation
433 detection methods BioCycle (Agostinelli et al., 2016) and MetaCycle (Wu et al., 2016).
434
435 **Quantitative reverse transcription polymerase chain reaction (qRT-PCR)**
436 Total RNA was extracted from cells and purified using the RNeasy Plus Micro Kit (Qiagen ,74034). 1μg of
437 total RNA was reverse transcribed using an oligo-dT primer and PrimeScript RTase (TaKaRa, Japan,
438 2680A). Quantitative real-time PCR was performed using a Rotor Gene Q (Qiagen) with TB Green Premix
439 Ex Taq (Takara, RR420A) The specific primers used were provided in the Table S3. Noncycling mRNA
440 encoding HPRT was used to normalize gene expression. The data were analyzed using Rotor Gene 6000
441 software, and the relative mRNA levels were quantified using the $2^{-\Delta\Delta Ct}$ method in which $\Delta\Delta Ct=[(Ct_{target} - Ct$
442 $_{HPRT})$ of experimental group]-[$(Ct_{target} - Ct_{HPRT})$ of control group].
443
444 **siRNA transfection and Immunoblotting**

The following On-Target plus SMARTpool siRNAs were purchased from Dharmacon (USA): Non-targeting CTRL siRNA (D-001810-01-50), *Herp* siRNA (L-049714-01-0005), *Itpr1* siRNA (L-040933-00-0005), and *Itpr2* siRNA (L-041018-00-0005). Upon reaching >90% confluence, the medium was replaced with serum-free MEM, and cells were incubated for 72hrs. Cells were then transfected with siRNA using Lipofectamine RNAiMAX (ThermoFisher, USA, 13778150) per the manufacturer's instructions. Experiments were conducted 48hrs post-transfection.

For immunoblotting, astrocytes were lysed using modified-RIPA buffer (50 mM Tris-HCl pH 7.4, 1% NP-40, 0.5% sodium deoxycholate, 150 mM NaCl). Mouse prefrontal cortex was lysed using T-Per (ThermoFisher, 78510) with protease inhibitor cocktail (Sigma-Aldrich, P8340) and phosphatase inhibitor cocktails 2 and 3 (Sigma-Aldrich, P5726 and P0044). Proteins were separated by SDS-PAGE and transferred to polyvinylidene fluoride membranes. Membranes were blocked with 5% skim milk and incubated overnight at 4°C with primary antibodies: anti-BMAL1 (Abcam (UK), ab93806), 1:2000; anti-HERP (Abcam, ab150424), 1:1000; anti-ITPR1 (Abcam, ab264284), 1:1000; anti-ITPR2 (Alomone Labs, Israel, ACC-116), 1:1000; anti-CX43 (Sigma, C6219), 1:5000; anti-pCX43 (Ser368) (CST, USA, 3511), 1:1000; anti-GAPDH (Novus, USA, NB100-56875), 1:5000; anti-vinculin (Sigma-Aldrich, V4505), 1:5000; and anti-total ERK (CST, 9102), 1:5000. Membranes were washed with TBST, incubated with secondary antibodies, and visualized using enhanced chemiluminescence. Protein levels were quantified by densitometric analysis of band intensities using ImageJ software.

Ca^{2+} reporter plasmid transfection and imaging analysis

After cells reached >90% confluence, the medium was replaced with serum-free MEM. For Ca^{2+} measurements, cells were transfected with Ca^{2+} indicator plasmids pCMV-G-CEPIA1er (a gift from Masamitsu Iino, Addgene plasmid #58215) (Suzuki et al., 2014), CMV-mito-R-GECO1, or CMV-R-GECO1 (gifts from Robert Campbell, Addgene plasmid #46021, #32444) (Wu et al., 2013) 72hrs post-serum deprivation using Lipofectamine 2000, with or without siRNA treatment. For Xestospongin C (XesC) experiments, 10 μM XesC was applied 30 minutes before imaging. 48hrs post-transfection, the medium was replaced with Ca^{2+}- and Mg^{2+}-free HBSS (Gibco, 14175095). Fluorescence images were captured every 3 seconds using a Nikon A1R Confocal Microscope with a x60 1.4 NA Plan-Apochromat objective at 37°C and 5% CO2. These experiments were conducted at the Three-Dimensional Immune System Imaging Core Facility of Ajou University (Korea). Images were analyzed using NIS Elements C software. Fluorescence intensity at each time point (F_t) and ΔF values (F_t-F_0) were calculated. F_0 values were averaged from the fluorescence intensity of 10 frames prior to stimulation.

Ca^{2+} reporter plasmid co-localization analysis

After cells reached >90% confluence, the medium was replaced with serum-free MEM. 72hrs later, cells were transfected with either the ER Ca^{2+} reporter plasmid pCMV-G-CEPIA1er or the mitochondrial Ca^{2+} reporter CMV-mito-R-GECO1. For ER co-localization analysis, pCMV-G-CEPIA1er was co-transfected with DsRed2-ER-5 (a gift from Michael Davidson, Addgene plasmid #55836) (Day & Davidson, 2009). For mitochondrial co-localization, 200 nM Mitotracker was applied 30 minutes before imaging. Live imaging was performed using a Nikon A1R Confocal Microscope with a x60 1.4 NA Plan-Apochromat objective at 37°C and 5% CO2. These experiments were conducted at the Three-Dimensional Immune System Imaging Core Facility of Ajou University (Korea). Images were analyzed using NIS Elements C software.

Gap-FRAP (fluorescence recovery after photobleaching) analysis

Astrocyte communication was evaluated using a modified gap-FRAP assay (Santiquet et al., 2012). 30 minutes before imaging, cells were incubated with 0.5 μM Calcein-AM (Invitrogen, C1430) and 0.05% Pluronic-127 (Invitrogen, P6866) at 37°C. After incubation, cells were rinsed twice with serum-free MEM to remove excess dye. For carbenoxolone (CBX) experiments, 20 μM CBX was added for 30 minutes after calcein incubation. Immediately before imaging, the medium was replaced with Ca^{2+}- and Mg^{2+}-free HBSS (Gibco, 14175095). Live imaging was performed using a Nikon A1R Confocal Microscope with a 488 nm argon laser and a x60 1.4 NA Plan-Apochromat objective. Photobleaching was performed on a region of interest (ROI) cell, and fluorescence was measured at 37°C and 5% CO2. Fluorescence intensity was recorded pre-bleach (5 images), during a 15-second laser pulse (100% power, 5.3 lines/sec), and post-bleach (every 3 seconds for 3 minutes). Images were analyzed using NIS Elements C software. Fluorescence intensity at each time point (F_t) was normalized to the pre-bleach intensity (F_0), calculated as the average of 5 pre-bleach frames. The percentage of fluorescence recovery was calculated using: (F_{FR}-

$F_A)/(F_0-F_A)$x100, where F_{FR} is the full recovery fluorescence intensity and F_A is the intensity immediately after photobleaching.

QUANTIFICATION AND STATISTICAL ANALYSIS

To conduct the statistical analyses, all samples were first tested for normality. For cases where normality testing was not possible, such as with the Area Under/Above Curve, *t*-tests were used for comparing two groups, and one-way ANOVA was used for comparing three or more groups, considering the sufficient sample size. When comparing two groups, a *t*-test was performed if the data followed a normal distribution; otherwise, the Mann-Whitney *U* test was used. For comparisons among three or more groups, one-way ANOVA was used if the data were normally distributed, and the Brown-Forsythe and Welch ANOVA tests were used if they were not. When comparing three or more groups across multiple time points, a two-way ANOVA was performed. A $p < 0.05$ was considered statistically significant for all tests.

Data and code availability

- Circadian RNA sequencing data have been deposited at GEO under accession number GEO: GSE254678.
- Any additional information required to reanalyze the data reported in this paper is available from the E.Y.K upon request.

Acknowledgments

We are very grateful to Eunhye Joe and all members of Eun Young Kim's laboratory for critical comments on the manuscript. This research was supported by National Research Foundation of Korea (NRF) grants funded by the Korean government (Ministry of Science and ICT; grant numbers, 2019M3C7A1031905, 2019R1A5A2026045).

Author Contributions

J.E.R., H.W.R., J.L., and E.Y.K designed research. J.E.R., K. S., H.W.R., and J.L. performed research. All authors analyzed data. J.E.R. and E.Y.K. wrote the first draft of the manuscript and all authors contributed to revising the manuscript.

Declaration of interests

The authors declare no competing interests.

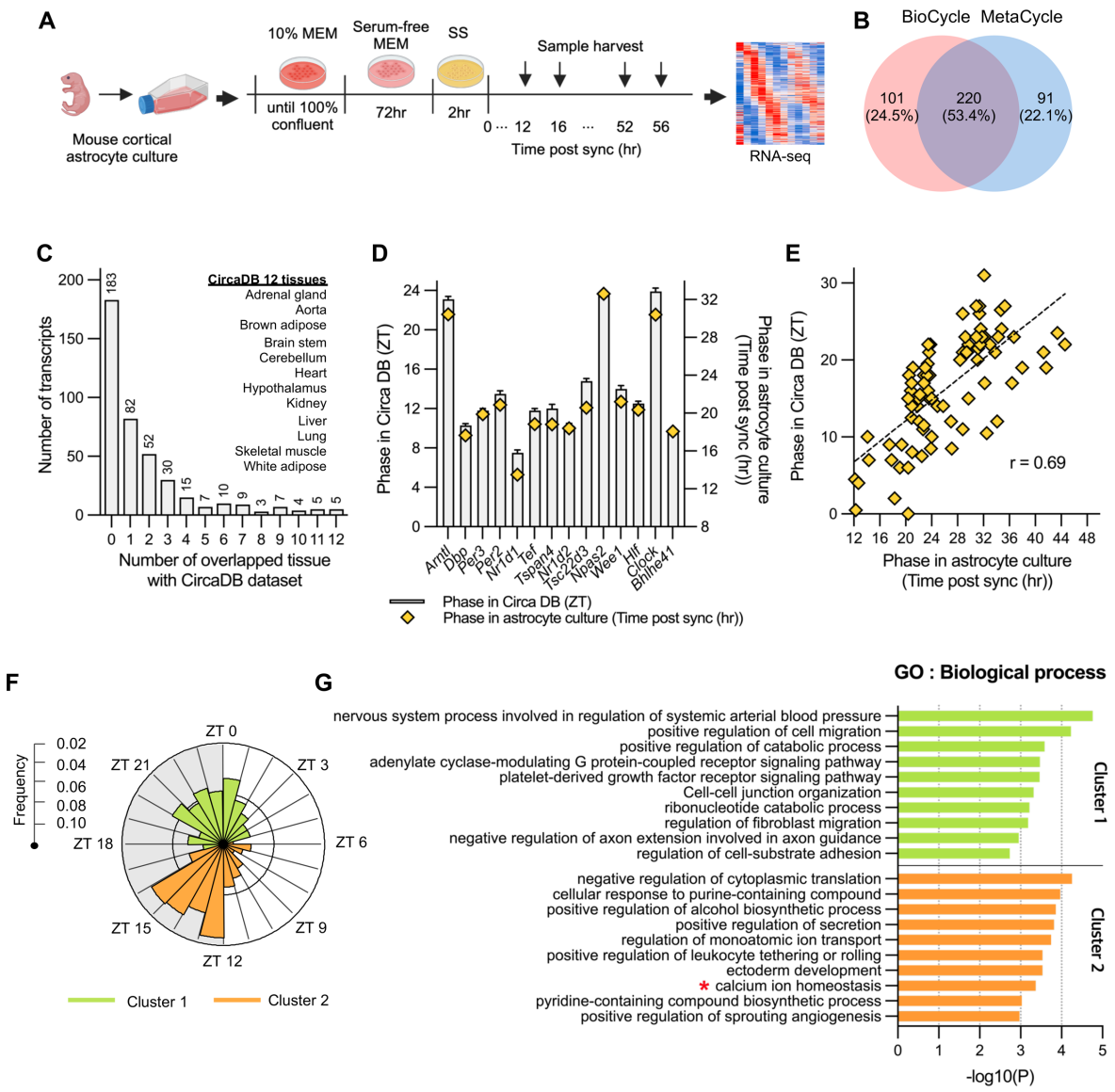

Figure 1. Circadian rhythmic transcripts in mouse cultured cortical astrocytes. (A) Experimental scheme for synchronizing circadian rhythms in mouse cultured cortical astrocytes followed by RNA-sequencing over 2 days. (B) Venn diagram displaying the number of circadian rhythmic transcripts identified by two algorithms ($q < 0.05$ in MetaCycle or BioCycle). (C) Number of transcripts that overlapping with 12 tissues in mouse circadian transcriptome ss from CircaDB (http://circadb.hogeneschlab.org). (D) Comparison of mean phase (ZT) from CircaDB and peak phase (Time post sync) from cultured astrocytes for 14 transcripts that are rhythmic in 10 or more tissues. (E) Scatter plot showing phase in CircaDB and peak phase of cultured astrocytes for transcripts that are rhythmic in one tissue. (F) Radial histogram of the distribution of phases of rhythmic genes in the astrocyte transcriptome. (G) Top 10 enriched GO Biological Process (BP) terms for significant circadian rhythmic genes in astrocytes ($p < 0.01$) identified by Metascape (https://metascape.org).

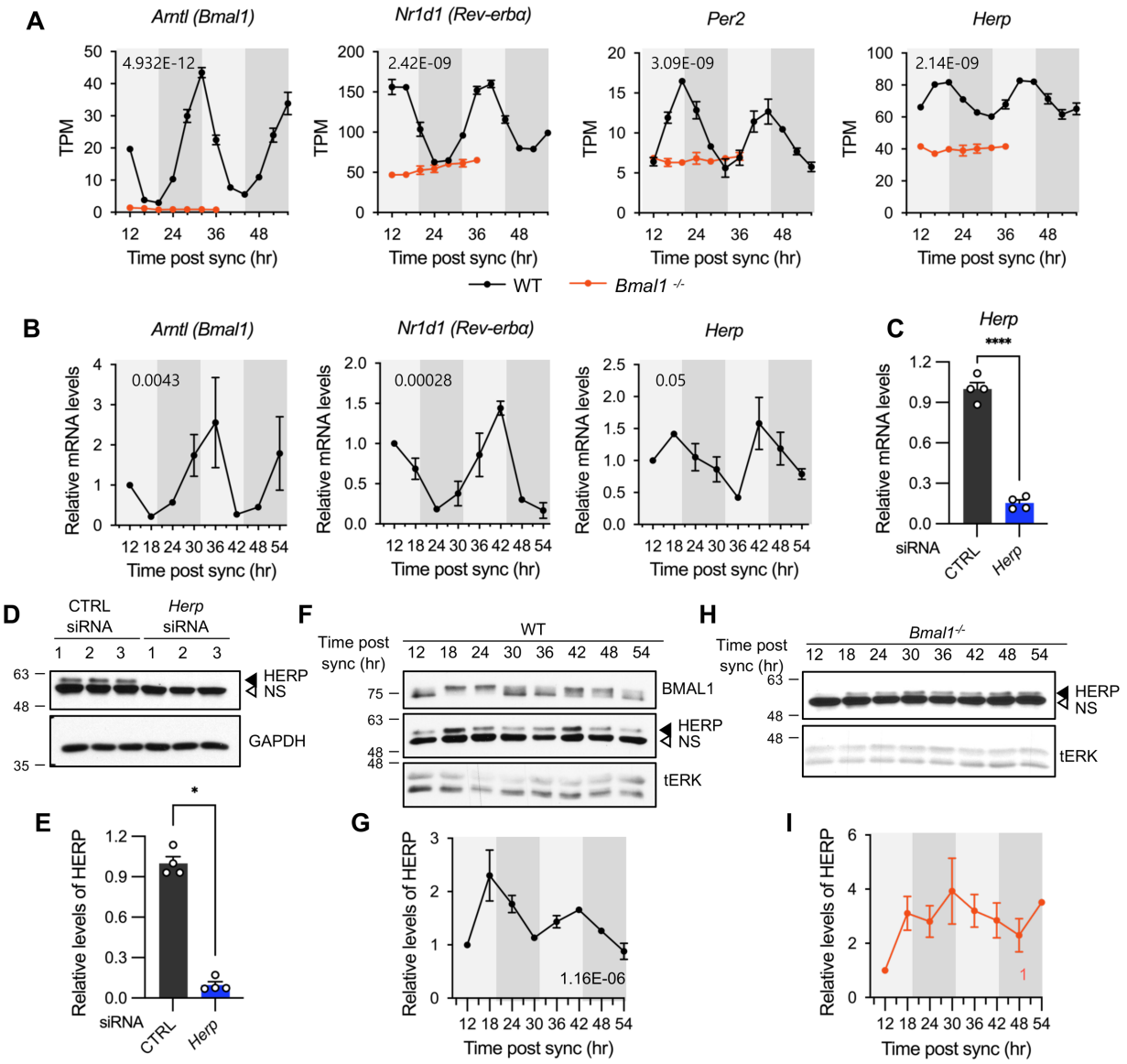

Figure 2. *Herp* is rhythmically expressed in mouse cultured astrocytes and its expression is controlled by BMAL1. (A, B) Astrocyte cultures from rom WT (black) and *Bmal1*$^{-/-}$ (orange) mice were synchronized and harvested at the indicated time. Expression was analyzed for rhythmicity using MetaCycle, and expression levels of given genes were quantified using RNA-seq (A) and real-time qRT-PCR (B) data. Values are mean ± SEM (n = 2; p-values are indicated by insets in graphs). Light gray and dark gray backgrounds represent subjective day and subjective night, respectively, based on the phase analysis from Figure 1D. (C-E) Cultured astrocytes were transfected with the indicated siRNA (20nM) and processed for real-time qRT-PCR (C) and Western blot (D, E) analyses at 48hrs post transfection. (C) Values are mean ± SEM (n = 4; **p* < 0.05, ***p* < 0.005, ****p* < 0.0005, and *****p* < 0.00005; *t*-test). (D) Representative Western blot images of four independent experiments are shown. GAPDH served as loading control. (E) Densitometric quantification of HERP levels, normalized to GAPDH levels. Values are mean ± SEM (n = 4; ****p* < 0.0005; Mann-Whiteny *U* test). (F-I) Astrocyte cultures from rom WT (F, G) and *Bmal1*$^{-/-}$ (H, I) mice were synchronized and harvested at the indicated time for Western blot analysis. Total ERK (tERK) served as a loading control. HERP/tERK values at different times were normalized to those at 12hr post sync (set to 1). Meta2d *p* values are indicated by insets in graphs. Light gray and dark gray backgrounds represent subjective day and subjective night, respectively. (F) Representative Western blot

images from five independent experiments are shown. (H) Representative Western blot images from two independent experiments are shown

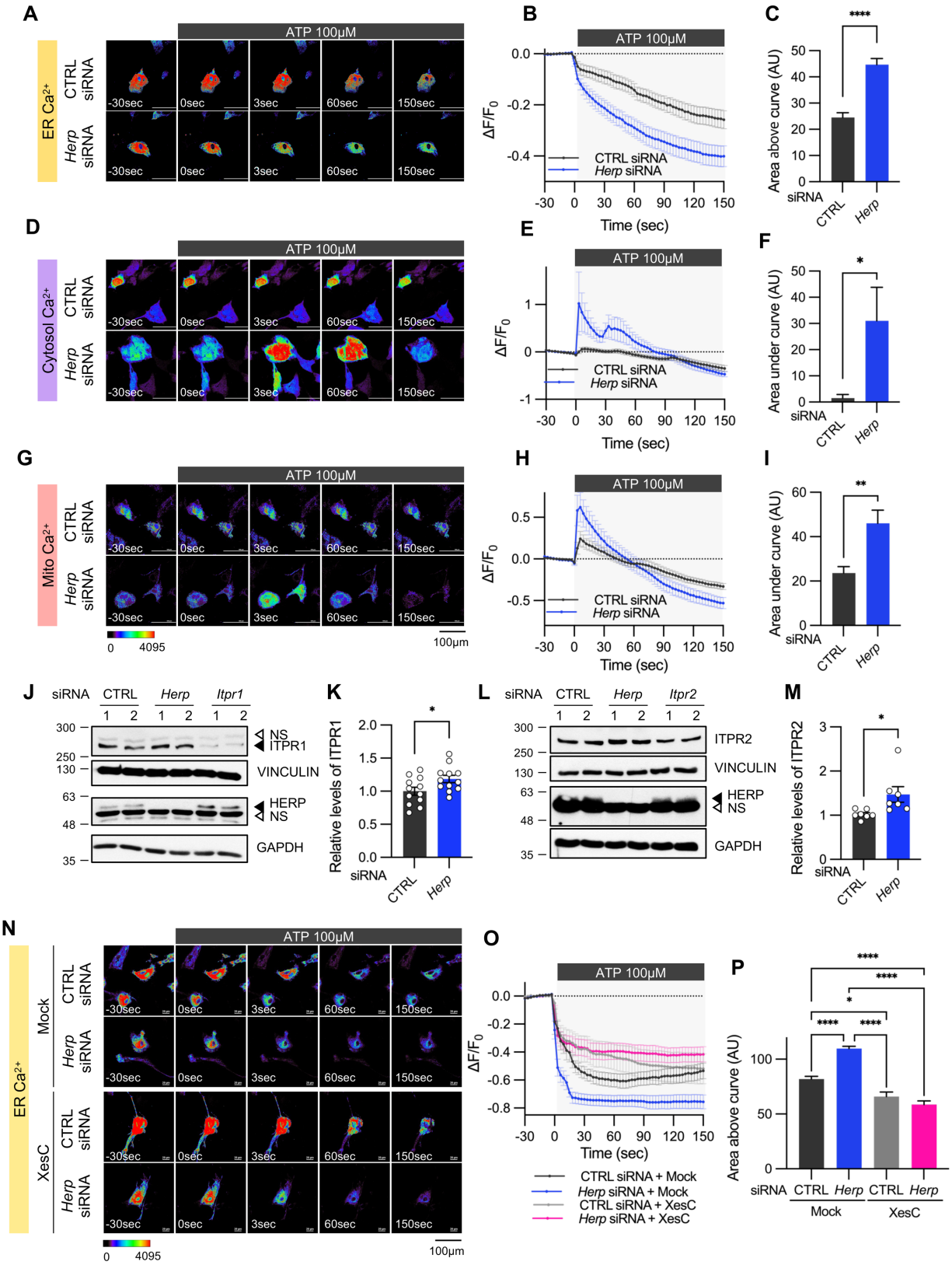

Figure 3. *Herp* knockdown altered ATP-induced ER Ca^{2+} response. (A-I) Cultured astrocytes were co-transfected with 20 μM non-targeting (CTRL) siRNA or *Herp* siRNA together with G-CEPIA1er (A-C), R-

GECO1 (D-F) or mito-R-GECO1 (G-I). At 48hrs post transfection, cultured astrocytes were treated with 100 μM ATP and Ca^{2+} imaging analysis was performed. Images were acquired every 3 seconds. (A, D, G) Representative time-lapse images of each Ca^{2+} indicator. (B, E, H) $\Delta F/F_0$ values over time following ATP application. (C, F, I) Area above or area under the curve values, calculated from panels B, E, and H. (A-C) CTRL siRNA, n = 19; *Herp* siRNA, n = 22. (D-F) CTRL siRNA, n = 20; *Herp* siRNA, n = 25. (G-I) CTRL siRNA, n = 16; *Herp* siRNA, n = 16. (J-M) Cultured astrocytes were transfected with the indicated siRNA (20nM) and processed for Western blot analysis 48hrs post transfection. Vinculin and GAPDH served as loading control for ITPRs and HERP, respectively. (J) Representative Western blot images from twelve independent experiments are shown. NS, non-specific band (K) Densitometric quantification of Western blot data showing relative levels of ITPR1 in *Herp* siRNA-transfected astrocytes compared to CTRL siRNA transfected astrocytes. (L) Representative Western blot images from five independent experiments. (M) Densitometric quantification of Western blot data showing relative levels of ITPR2 in *Herp* siRNA-transfected astrocytes compared to Control astrocytes. Values are mean ± SEM (*$p < 0.05$, **$p < 0.005$, ***$p < 0.0005$, ****$p < 0.00005$; *t*-test). (N-P) Cultured astrocytes were treated with 10μM Xestospongin C (XesC), an IP3R inhibitor, for 30 minutes before live imaging. Cells were then treated with 100μM ATP, and images were captured every 3 seconds. (N) Representative time-lapse images of ER Ca^{2+} indicator. (O) $\Delta F/F_0$ values over time following ATP application. (P) Area above the curve values were calculated from panel B. CTRL siRNA + Mock, n = 9; *Herp* siRNA + Mock, n = 9 ; CTRL siRNA + XesC, n = 8; *Herp* siRNA + XesC, n = 14. Values are means ± SEM (*$p < 0.05$, **$p < 0.005$, ***$p < 0.0005$, ****$p < 0.00005$; one-way ANOVA).

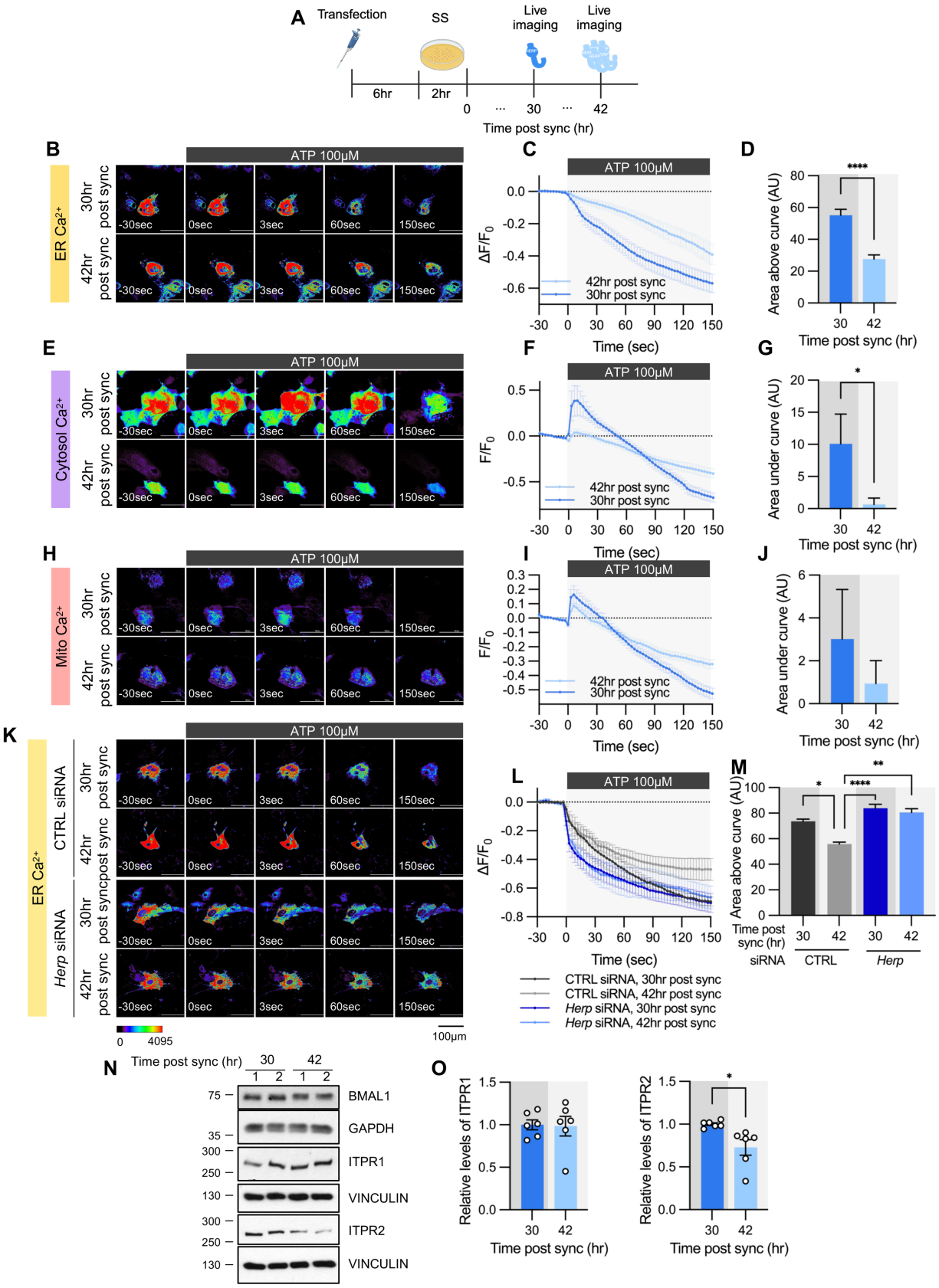

Figure 4. ATP-induced ER Ca^{2+} release varies according to time post sync. (A) Schematic diagram of

the experimental scheme from transfection to live-cell Ca^{2+} imaging at different times. (B-M) Cultured astrocytes were transfected with G-CEPIA1er (B-D, K-M), R-GECO1 (E-G), or mito-R-GECO1 (H-J) compartment-specific Ca^{2+} indicators (denoted at left) and then their circadian rhythm was synchronized by SS. (K-M) The indicated siRNA was co-transfected with the ER Ca^{2+} indicator. After transfection, cells were allowed 48hrs for the siRNA to take effect and stabilize before synchronization by serum shock. At the indicated times, astrocytes were treated with 100 μM ATP and Ca^{2+} imaging was performed. (B, E, H, K) Representative time-lapse images of each Ca^{2+} indicator. (C, F, I, L) $\Delta F/F_0$ values over time following ATP application. (D, G, J, M) Area above or area under the curve values, calculated from panels C, F, I, and L. (B-D) 30hr post sync, n = 24; 42hr post sync, n = 19. (E-G) 30hr post sync, n = 33; 42hr post sync, n = 38. (H-J) 30hr post sync, n = 50; 42hr post sync, n = 54. (K-M) CTRL siRNA, 30hr post sync, n = 5; CTRL siRNA, 42hr post sync, n = 4; *Herp* siRNA, 30hr post sync, n = 11; *Herp* siRNA, 42hr post sync, n = 5. Values in graphs are mean ± SEM (*$p < 0.05$, ****$p < 0.00005$; (D, G, J) *t*-test, (M) one-way ANOVA. (N-O) Cells were harvested at the indicated times and processed for Western blot analysis. Vinculin and GAPDH served as loading controls for ITPR and BMAL1, respectively. (N) Representative Western blot images from six independent experiments. (O) Densitometric quantification of Western blot data showing relative levels of ITPR1 and ITPR2 at different times. Values in graphs are mean ± SEMs (*$p < 0.05$, ****$p < 0.00005$; *t*-test).

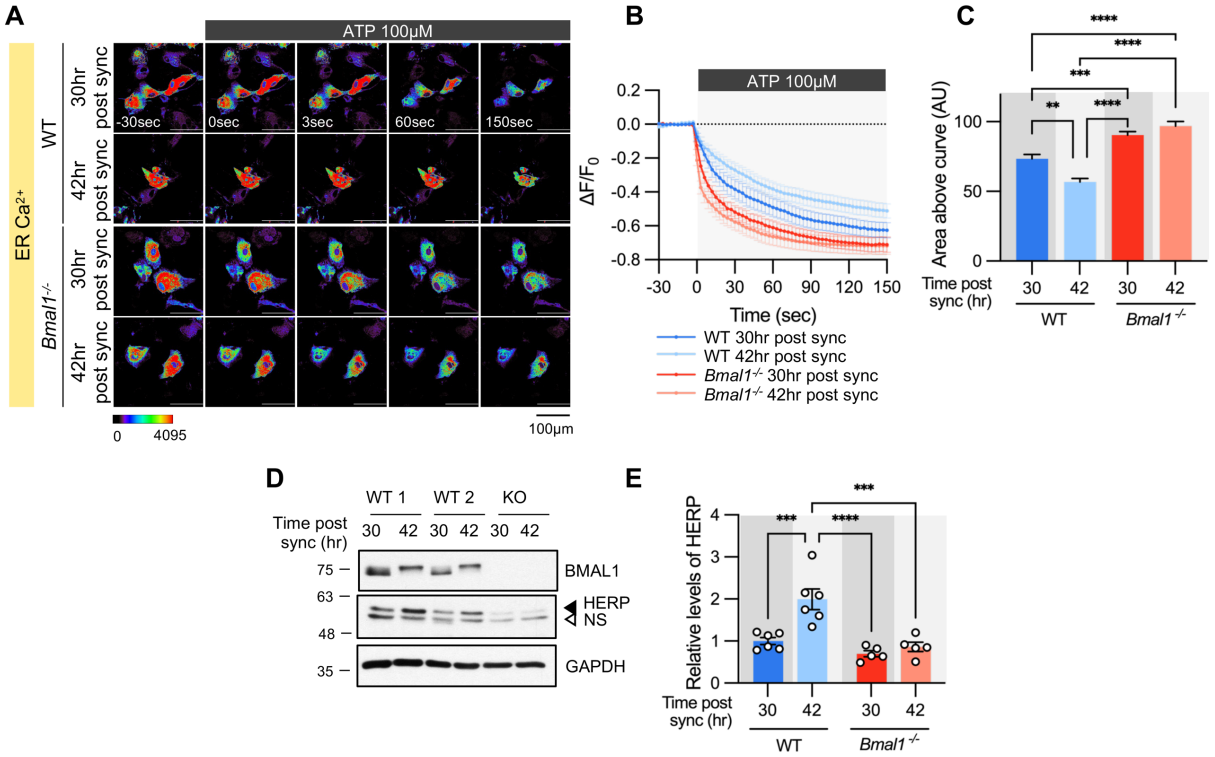

Figure 5. Time-dependent ER Ca^{2+} release is abolished in cultured astrocytes from *Bmal1*$^{-/-}$ mice. Cultured astrocytes *Bmal1*$^{-/-}$ mice and WT littermates were transfected with G-CEPIA1er and then their circadian rhythm was synchronized by SS. At the indicated Time, astrocytes were treated with 100 μM ATP and Ca^{2+} imaging was performed. (A) Representative time-lapse images of ER Ca^{2+} indicator. (B) $\Delta F/F_0$ values over time following ATP application. (C) Area above the curve values, calculated from panel B. (A-C) WT 30hr post sync, n = 17; WT 42hr post sync, n = 15; KO 30hr post sync, n = 19; KO 42hr post sync, n = 21. Values are mean ± SEM (*$p < 0.05$, **$p < 0.005$, ***$p < 0.0005$, ****$p < 0.00005$; one-way ANOVA). (D, E) Cultured astrocytes from *Bmal1*$^{-/-}$ mice and WT littermates were synchronized by SS. Cells were harvested at the indicated times and processed for Western blot analysis. (D) Representative Western blot images from six independent experiments. GAPDH served as a loading control. (E) Values are mean ± SEM (*$p < 0.05$, **$p < 0.005$, ***$p < 0.0005$, ****$p < 0.00005$; two-way ANOVA).

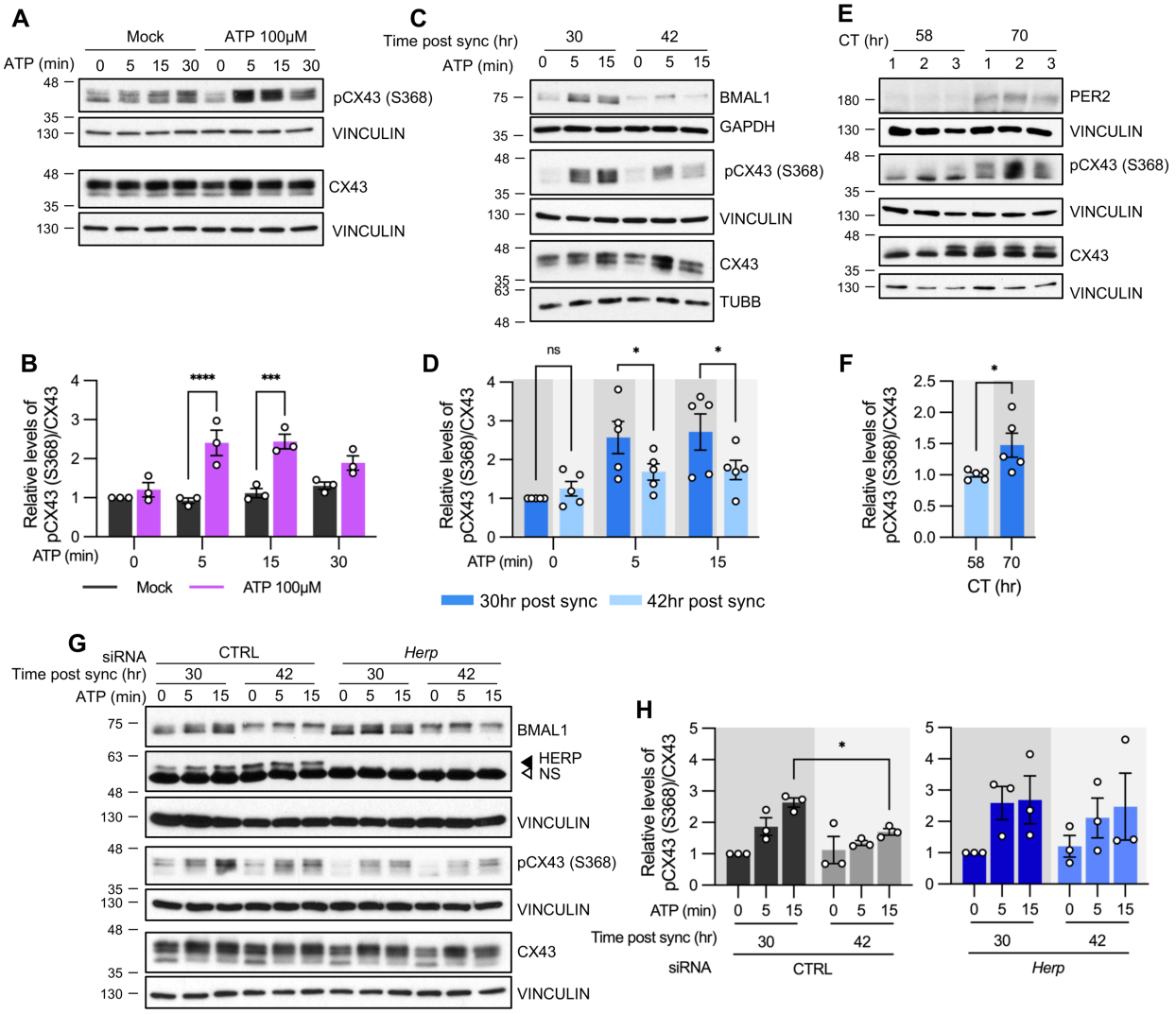

Figure 6. ATP-induced pCX43 (S368) levels varies according to time post sync. (A-D, G, H) Cultured astrocytes with (C, D) or without (A, B) synchronization, were treated with 100 μM ATP either at 30hr post sync or 42hr post sync and processed for Western blot analysis at the indicated times. Vinculin, GAPDH, and/or β-tubulin (TUBB) served as loading controls. The intensity of pCX43 (S368) and Cx43 for each sample was normalized to that of Vinculin. (A) Representative Western blot images from more three independent experiments. Vinculin served as a loading control. (B) Densitometric quantification of Western blot data, showing relative pCX43 (S368)/CX43 levels. Values are normalized to those for mock-treated samples at time zero (set to 1). (C) Representative Western blot images from three independent experiments. Vinculin, GAPDH, and β-tubulin (TUBB) served as loading controls. (D) Densitometric quantification of Western blot data, showing relative pCX43 (S368)/CX43 levels. Values are normalized to those for mock-treated samples at ATP zero for 30hr post sync (set to 1). (E, F) Changes in CX43 phosphorylation in vivo. Mice were entrained to a 12-hour light/dark cycle followed by constant dark conditions. At the indicated times, the prefrontal cortex area was dissected and processed for Western blot analysis. (E) Representative Western blot images from three independent experiments. (F) Densitometric quantification of Western blot data showing relative levels of pCX43 (S368). (G, H) 48hrs post siRNA transfection, cells were synchronized by serum shock. At the indicated times post sync, 100 μM ATP was treated and processed for Western blot analysis (G) Representative Western blot images from three independent experiments. Vinculin served as a loading control. (H) Densitometric quantification of Western blot data, showing relative pCX43 (S368)/CX43 levels. Values are normalized to those for 30hr post sync

652 at ATP zero (min) (set to 1). Values are mean ± SEM (*$p < 0.05$, **$p < 0.005$, ***$p < 0.0005$, ****$p < 0.00005$;
653 (B, D, H) two-way ANOVA, (F) *t*-test).
654
655

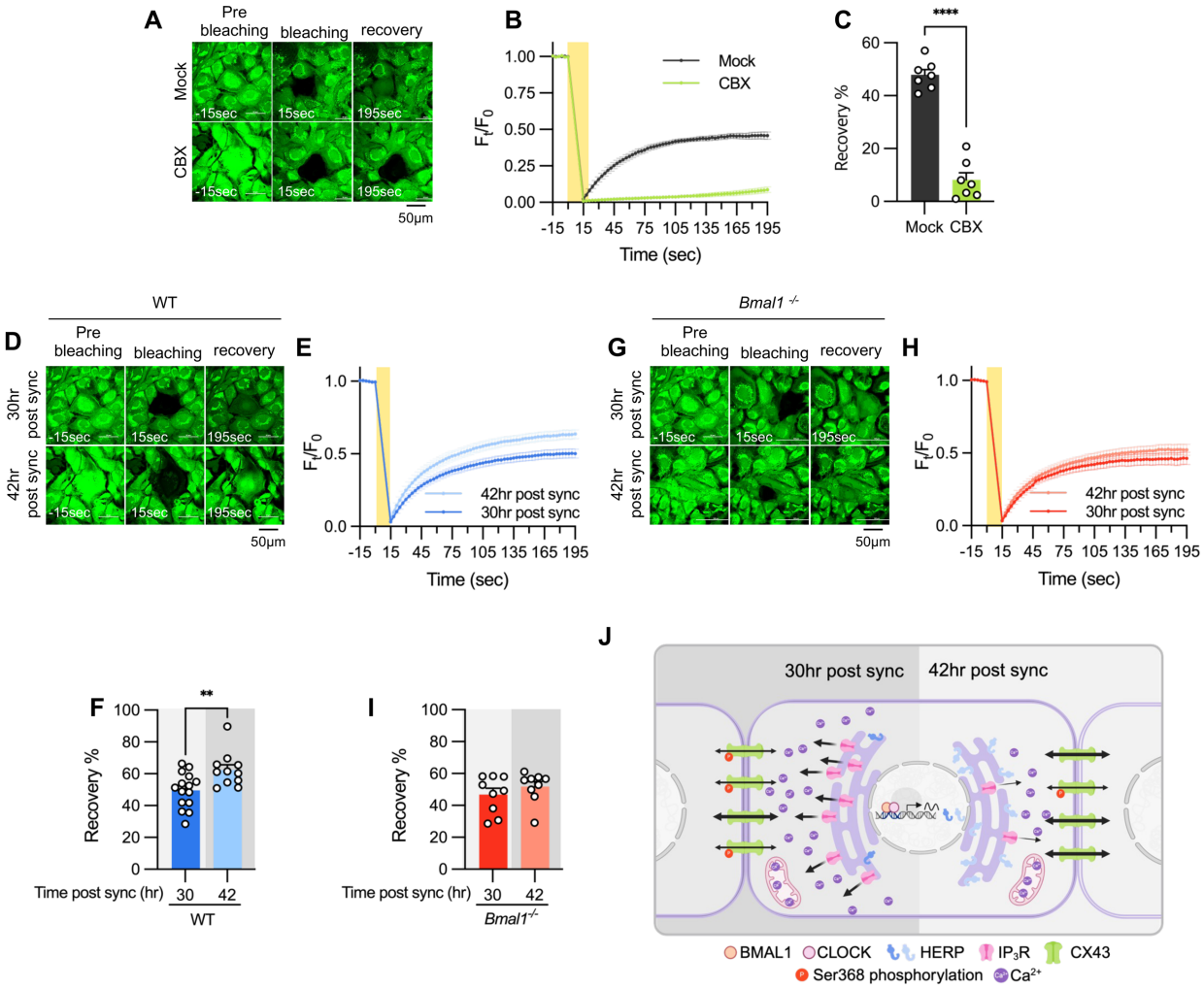

Figure 7. Gap junction conductance varies according to time post sync.
(A- C) 20μM carbenoxolone (CBX), a gap junction channel block, was applied to cultured astrocytes for 30 minutes before gap-FRAP analysis. (A) Representative time-lapse images of prebleaching, bleaching and recovery condition during gap-FRAP analysis. (B) F_t/F_0 values over time following photobleaching (yellow rectangle). (C) Recovery % values, calculated from panel B. Mock, n = 7; CBX, n = 7. Values in graphs are mean ± SEM (*p < 0.05, **p < 0.005, ***p < 0.0005, and ****p < 0.00005; Mann-Whitney U test). (D-I) Cultured astrocytes from WT (D-F) and *Bmal1*$^{-/-}$ (G-I) mice were synchronized by SS. At the indicated time, gap-FRAP was performed. (D, G) Representative time-lapse images of prebleaching, bleaching and recovery condition during gap-FRAP analysis at 30hr post sync and 42hr post sync. (E, H) F_t/F_0 values over time following photobleaching (yellow rectangle). (F and I) Recovery % values, calculated from panel H and L, respectively. (D-F) 30hr post sync, n = 15; 42hr post sync, n = 11. (G-I) 30hr post sync, n = 9; 42hr post sync, n = 9. Values in graphs are mean ± SEM (*p < 0.05, **p < 0.005, ***p < 0.0005, and ****p < 0.00005; F : t-test, I : Mann-Whiteny U test). (J) Schematic diagram illustrating the regulation of ER Ca^{2+} response by the circadian clock through rhythmic oscillation of HERP. Refer to the text for the detailed explanation.

References

Agostinelli, F., Ceglia, N., Shahbaba, B., Sassone-Corsi, P., & Baldi, P. (2016). What time is it? Deep learning approaches for circadian rhythms. *Bioinformatics*, *32*(12), i8-i17. https://doi.org/10.1093/bioinformatics/btw243

Agulhon, C., Petravicz, J., McMullen, A. B., Sweger, E. J., Minton, S. K., Taves, S. R., Casper, K. B., Fiacco, T. A., & McCarthy, K. D. (2008). What Is the Role of Astrocyte Calcium in Neurophysiology? *Neuron*, *59*(6), 932-946. https://doi.org/https://doi.org/10.1016/j.neuron.2008.09.004

Annayev, Y., Adar, S., Chiou, Y. Y., Lieb, J. D., Sancar, A., & Ye, R. (2014). Gene model 129 (Gm129) encodes a novel transcriptional repressor that modulates circadian gene expression. *J Biol Chem*, *289*(8), 5013-5024. https://doi.org/10.1074/jbc.M113.534651

Balsalobre, A., Brown, S. A., Marcacci, L., Tronche, F., Kellendonk, C., Reichardt, H. M., Schütz, G., & Schibler, U. (2000). Resetting of circadian time in peripheral tissues by glucocorticoid signaling. *Science*, *289*(5488), 2344-2347. https://doi.org/10.1126/science.289.5488.2344

Balsalobre, A., Damiola, F., & Schibler, U. (1998). A serum shock induces circadian gene expression in mammalian tissue culture cells. *Cell*, *93*(6), 929-937. https://doi.org/10.1016/s0092-8674(00)81199-x

Barca-Mayo, O., Boender, A. J., Armirotti, A., & De Pietri Tonelli, D. (2020). Deletion of astrocytic BMAL1 results in metabolic imbalance and shorter lifespan in mice. *Glia*, *68*(6), 1131-1147. https://doi.org/10.1002/glia.23764

Barca-Mayo, O., Pons-Espinal, M., Follert, P., Armirotti, A., Berdondini, L., & De Pietri Tonelli, D. (2017). Astrocyte deletion of Bmal1 alters daily locomotor activity and cognitive functions via GABA signalling. *Nat Commun*, *8*, 14336. https://doi.org/10.1038/ncomms14336

Baryshnikov, S. G., Rogachevskaja, O. A., & Kolesnikov, S. S. (2003). Calcium signaling mediated by P2Y receptors in mouse taste cells. *J Neurophysiol*, *90*(5), 3283-3294. https://doi.org/10.1152/jn.00312.2003

Bell-Pedersen, D., Cassone, V. M., Earnest, D. J., Golden, S. S., Hardin, P. E., Thomas, T. L., & Zoran, M. J. (2005). Circadian rhythms from multiple oscillators: lessons from diverse organisms. *Nat Rev Genet*, *6*(7), 544-556. https://doi.org/10.1038/nrg1633

Blum, I. D., Keleş, M. F., Baz, E. S., Han, E., Park, K., Luu, S., Issa, H., Brown, M., Ho, M. C. W., Tabuchi, M., Liu, S., & Wu, M. N. (2021). Astroglial Calcium Signaling Encodes Sleep Need in Drosophila. *Curr Biol*, *31*(1), 150-162.e157. https://doi.org/10.1016/j.cub.2020.10.012

Bojarskaite, L., Bjornstad, D. M., Pettersen, K. H., Cunen, C., Hermansen, G. H., Abjorsbraten, K. S., Chambers, A. R., Sprengel, R., Vervaeke, K., Tang, W., Enger, R., & Nagelhus, E. A. (2020). Astrocytic Ca(2+) signaling is reduced during sleep and is involved in the regulation of slow wave sleep. *Nat Commun*, *11*(1), 3240. https://doi.org/10.1038/s41467-020-17062-2

Brancaccio, M., Edwards, M. D., Patton, A. P., Smyllie, N. J., Chesham, J. E., Maywood, E. S., & Hastings, M. H. (2019). Cell-autonomous clock of astrocytes drives circadian behavior in mammals. *Science*, *363*(6423), 187-192. https://doi.org/10.1126/science.aat4104

Brancaccio, M., Patton, A. P., Chesham, J. E., Maywood, E. S., & Hastings, M. H. (2017). Astrocytes Control Circadian Timekeeping in the Suprachiasmatic Nucleus via Glutamatergic Signaling. *Neuron*, *93*(6), 1420-1435 e1425. https://doi.org/10.1016/j.neuron.2017.02.030

Brandebura, A. N., Paumier, A., Onur, T. S., & Allen, N. J. (2023). Astrocyte contribution to dysfunction, risk and progression in neurodegenerative disorders. *Nature Reviews Neuroscience*, *24*(1), 23-39. https://doi.org/10.1038/s41583-022-00641-1

Bunger, M. K., Wilsbacher, L. D., Moran, S. M., Clendenin, C., Radcliffe, L. A., Hogenesch, J. B., Simon, M. C., Takahashi, J. S., & Bradfield, C. A. (2000). Mop3 is an essential component of the master circadian pacemaker in mammals. *Cell*, *103*(7), 1009-1017. https://doi.org/10.1016/s0092-8674(00)00205-1

Carreras-Sureda, A., Pihán, P., & Hetz, C. (2018). Calcium signaling at the endoplasmic reticulum: fine-tuning stress responses. *Cell Calcium*, *70*, 24-31. https://doi.org/https://doi.org/10.1016/j.ceca.2017.08.004

Choi, D. J., Eun, J. H., Kim, B. G., Jou, I., Park, S. M., & Joe, E. H. (2018). A Parkinson's disease gene, DJ-1, repairs brain injury through Sox9 stabilization and astrogliosis. *Glia*, *66*(2), 445-458. https://doi.org/10.1002/glia.23258

Day, R. N., & Davidson, M. W. (2009). The fluorescent protein palette: tools for cellular imaging. *Chem Soc Rev*, *38*(10), 2887-2921. https://doi.org/10.1039/b901966a

Dobin, A., Davis, C. A., Schlesinger, F., Drenkow, J., Zaleski, C., Jha, S., Batut, P., Chaisson, M., & Gingeras, T. R. (2013). STAR: ultrafast universal RNA-seq aligner. *Bioinformatics*, *29*(1), 15-21. https://doi.org/10.1093/bioinformatics/bts635

Enkvist, M. O., & McCarthy, K. D. (1992). Activation of protein kinase C blocks astroglial gap junction communication and inhibits the spread of calcium waves. *J Neurochem*, *59*(2), 519-526. https://doi.org/10.1111/j.1471-4159.1992.tb09401.x

Fujii, Y., Maekawa, S., & Morita, M. (2017). Astrocyte calcium waves propagate proximally by gap junction and distally by extracellular diffusion of ATP released from volume-regulated anion channels. *Scientific Reports*, *7*(1), 13115. https://doi.org/10.1038/s41598-017-13243-0

Giaume, C., Naus, C. C., Sáez, J. C., & Leybaert, L. (2021). Glial Connexins and Pannexins in the Healthy and Diseased Brain. *Physiol Rev*, *101*(1), 93-145. https://doi.org/10.1152/physrev.00043.2018

Giorgi, C., Marchi, S., & Pinton, P. (2018). The machineries, regulation and cellular functions of mitochondrial calcium. *Nature Reviews Molecular Cell Biology*, *19*(11), 713-730. https://doi.org/10.1038/s41580-018-0052-8

Glynn, E. F., Chen, J., & Mushegian, A. R. (2006). Detecting periodic patterns in unevenly spaced gene expression time series using Lomb-Scargle periodograms. *Bioinformatics*, *22*(3), 310-316. https://doi.org/10.1093/bioinformatics/bti789

Griffin, P., Dimitry, J. M., Sheehan, P. W., Lananna, B. V., Guo, C., Robinette, M. L., Hayes, M. E., Cedeno, M. R., Nadarajah, C. J., Ezerskiy, L. A., Colonna, M., Zhang, J., Bauer, A. Q., Burris, T. P., & Musiek, E. S. (2019). Circadian clock protein Rev-erbalpha regulates neuroinflammation. *Proc Natl Acad Sci U S A*, *116*(11), 5102-5107. https://doi.org/10.1073/pnas.1812405116

Guerra-Gomes, S., Sousa, N., Pinto, L., & Oliveira, J. F. (2017). Functional Roles of Astrocyte Calcium Elevations: From Synapses to Behavior. *Front Cell Neurosci*, *11*, 427. https://doi.org/10.3389/fncel.2017.00427

Hong, H. K., Maury, E., Ramsey, K. M., Perelis, M., Marcheva, B., Omura, C., Kobayashi, Y., Guttridge, D. C., Barish, G. D., & Bass, J. (2018). Requirement for NF-κB in maintenance of molecular and behavioral circadian rhythms in mice. *Genes Dev*, *32*(21-22), 1367-1379. https://doi.org/10.1101/gad.319228.118

Hughes, M. E., Hogenesch, J. B., & Kornacker, K. (2010). JTK_CYCLE: an efficient nonparametric algorithm for detecting rhythmic components in genome-scale data sets. *J Biol Rhythms*, *25*(5), 372-380. https://doi.org/10.1177/0748730410379711

Ingiosi, A. M., Hayworth, C. R., Harvey, D. O., Singletary, K. G., Rempe, M. J., Wisor, J. P., & Frank, M. G. (2020). A Role for Astroglial Calcium in Mammalian Sleep and Sleep Regulation. *Curr Biol*, *30*(22), 4373-4383.e4377. https://doi.org/10.1016/j.cub.2020.08.052

James, G., & Butt, A. M. (2001). P2X and P2Y purinoreceptors mediate ATP-evoked calcium signalling in optic nerve glia in situ. *Cell Calcium*, *30*(4), 251-259. https://doi.org/10.1054/ceca.2001.0232

Kokame, K., Agarwala, K. L., Kato, H., & Miyata, T. (2000). Herp, a new ubiquitin-like membrane protein induced by endoplasmic reticulum stress. *J Biol Chem*, *275*(42), 32846-32853. https://doi.org/10.1074/jbc.M002063200

Kokame, K., Kato, H., & Miyata, T. (1996). Homocysteine-respondent genes in vascular endothelial cells identified by differential display analysis. GRP78/BiP and novel genes. *J Biol Chem*, *271*(47), 29659-29665. https://doi.org/10.1074/jbc.271.47.29659

Kunzelmann, P., Schroder, W., Traub, O., Steinhauser, C., Dermietzel, R., & Willecke, K. (1999). Late onset and increasing expression of the gap junction protein connexin30 in adult murine brain and long-term cultured astrocytes. *Glia*, *25*(2), 111-119. https://doi.org/10.1002/(sici)1098-1136(19990115)25:2<111::aid-glia2>3.0.co;2-i

Lananna, B. V., & Musiek, E. S. (2020). The wrinkling of time: Aging, inflammation, oxidative stress, and the circadian clock in neurodegeneration. *Neurobiol Dis*, *139*, 104832. https://doi.org/10.1016/j.nbd.2020.104832

Lananna, B. V., Nadarajah, C. J., Izumo, M., Cedeno, M. R., Xiong, D. D., Dimitry, J., Tso, C. F., McKee, C. A., Griffin, P., Sheehan, P. W., Haspel, J. A., Barres, B. A., Liddelow, S. A., Takahashi, J. S., Karatsoreos, I. N., & Musiek, E. S. (2018). Cell-Autonomous Regulation of Astrocyte Activation by the Circadian Clock Protein BMAL1. *Cell Rep*, *25*(1), 1-9 e5. https://doi.org/10.1016/j.celrep.2018.09.015

Langer, J., Stephan, J., Theis, M., & Rose, C. R. (2012). Gap junctions mediate intercellular spread of sodium between hippocampal astrocytes in situ. *Glia*, *60*(2), 239-252. https://doi.org/10.1002/glia.21259

Leitman, J., Shenkman, M., Gofman, Y., Shtern, N. O., Ben-Tal, N., Hendershot, L. M., & Lederkremer, G. Z. (2014). Herp coordinates compartmentalization and recruitment of HRD1 and misfolded proteins for ERAD. *Mol Biol Cell*, *25*(7), 1050-1060. https://doi.org/10.1091/mbc.E13-06-0350

Marpegan, L., Krall, T. J., & Herzog, E. D. (2009). Vasoactive intestinal polypeptide entrains circadian rhythms in astrocytes. *J Biol Rhythms*, *24*(2), 135-143. https://doi.org/10.1177/0748730409332042

Mei, W., Jiang, Z., Chen, Y., Chen, L., Sancar, A., & Jiang, Y. (2020). Genome-wide circadian rhythm detection methods: systematic evaluations and practical guidelines. *Briefings in Bioinformatics*, *22*(3). https://doi.org/10.1093/bib/bbaa135

Metsalu, T., & Vilo, J. (2015). ClustVis: a web tool for visualizing clustering of multivariate data using Principal Component Analysis and heatmap. *Nucleic Acids Res*, *43*(W1), W566-570. https://doi.org/10.1093/nar/gkv468

Mohawk, J. A., Green, C. B., & Takahashi, J. S. (2012). Central and peripheral circadian clocks in mammals. *Annu Rev Neurosci*, *35*, 445-462. https://doi.org/10.1146/annurev-neuro-060909-153128

Mure, L. S., Le, H. D., Benegiamo, G., Chang, M. W., Rios, L., Jillani, N., Ngotho, M., Kariuki, T., Dkhissi-Benyahya, O., Cooper, H. M., & Panda, S. (2018). Diurnal transcriptome atlas of a primate across major neural and peripheral tissues. *Science*, *359*(6381). https://doi.org/10.1126/science.aao0318

Nagy, J. I., Patel, D., Ochalski, P. A., & Stelmack, G. L. (1999). Connexin30 in rodent, cat and human brain: selective expression in gray matter astrocytes, co-localization with connexin43 at gap junctions and late developmental appearance. *Neuroscience*, *88*(2), 447-468. https://doi.org/10.1016/s0306-4522(98)00191-2

Neary, J. T., van Breemen, C., Forster, E., Norenberg, L. O., & Norenberg, M. D. (1988). ATP stimulates calcium influx in primary astrocyte cultures. *Biochem Biophys Res Commun*, *157*(3), 1410-1416. https://doi.org/10.1016/s0006-291x(88)81032-5

Nimlamool, W., Andrews, R. M., & Falk, M. M. (2015). Connexin43 phosphorylation by PKC and MAPK signals VEGF-mediated gap junction internalization. *Mol Biol Cell*, *26*(15), 2755-2768. https://doi.org/10.1091/mbc.E14-06-1105

Oki, S., Ohta, T., Shioi, G., Hatanaka, H., Ogasawara, O., Okuda, Y., Kawaji, H., Nakaki, R., Sese, J., & Meno, C. (2018). ChIP-Atlas: a data-mining suite powered by full integration of public ChIP-seq data. *EMBO reports*, *19*(12), e46255. https://doi.org/https://doi.org/10.15252/embr.201846255

Pacholko, A. G., Wotton, C. A., & Bekar, L. K. (2020). Astrocytes—The Ultimate Effectors of Long-Range Neuromodulatory Networks? [Review]. *Frontiers in Cellular Neuroscience*, *14*. https://doi.org/10.3389/fncel.2020.581075

Panda, S., Antoch, M. P., Miller, B. H., Su, A. I., Schook, A. B., Straume, M., Schultz, P. G., Kay, S. A., Takahashi, J. S., & Hogenesch, J. B. (2002). Coordinated transcription of key pathways in the mouse by the circadian clock. *Cell*, *109*(3), 307-320. https://doi.org/10.1016/s0092-8674(02)00722-5

Paredes, F., Parra, V., Torrealba, N., Navarro-Marquez, M., Gatica, D., Bravo-Sagua, R., Troncoso, R., Pennanen, C., Quiroga, C., Chiong, M., Caesar, C., Taylor, W. R., Molgó, J., San Martin, A., Jaimovich, E., & Lavandero, S. (2016). HERPUD1 protects against oxidative stress-induced apoptosis through downregulation of the inositol 1,4,5-trisphosphate receptor. *Free Radic Biol Med*, *90*, 206-218. https://doi.org/10.1016/j.freeradbiomed.2015.11.024

Patton, A. P., Smyllie, N. J., Chesham, J. E., & Hastings, M. H. (2022). Astrocytes sustain circadian oscillation and bidirectionally determine circadian period, but do not regulate circadian phase in the suprachiasmatic nucleus. *J Neurosci*, *42*(28), 5522-5537. https://doi.org/10.1523/jneurosci.2337-21.2022

Phatnani, H., & Maniatis, T. (2015). Astrocytes in neurodegenerative disease. *Cold Spring Harb Perspect Biol*, *7*(6). https://doi.org/10.1101/cshperspect.a020628

Prolo, L. M., Takahashi, J. S., & Herzog, E. D. (2005). Circadian Rhythm Generation and Entrainment in Astrocytes. *The Journal of Neuroscience*, *25*(2), 404-408. https://doi.org/10.1523/jneurosci.4133-04.2005

Rakshit, K., Qian, J., Ernst, J., & Matveyenko, A. V. (2016). Circadian variation of the pancreatic islet transcriptome. *Physiological Genomics*, *48*(9), 677-687. https://doi.org/10.1152/physiolgenomics.00019.2016

Reddy, A. B., Karp, N. A., Maywood, E. S., Sage, E. A., Deery, M., O'Neill, J. S., Wong, G. K., Chesham, J., Odell, M., Lilley, K. S., Kyriacou, C. P., & Hastings, M. H. (2006). Circadian orchestration of the hepatic proteome. *Curr Biol*, *16*(11), 1107-1115. https://doi.org/10.1016/j.cub.2006.04.026

Reinke, H., & Asher, G. (2019). Crosstalk between metabolism and circadian clocks. *Nat Rev Mol Cell Biol*, *20*(4), 227-241. https://doi.org/10.1038/s41580-018-0096-9

Schultz, T. F., & Kay, S. A. (2003). Circadian clocks in daily and seasonal control of development. *Science*, *301*(5631), 326-328. https://doi.org/10.1126/science.1085935

Sofroniew, M. V., & Vinters, H. V. (2010). Astrocytes: biology and pathology. *Acta Neuropathol*, *119*(1), 7-35. https://doi.org/10.1007/s00401-009-0619-8

Solan, J. L., & Lampe, P. D. (2014). Specific Cx43 phosphorylation events regulate gap junction turnover in vivo. *FEBS Lett*, *588*(8), 1423-1429. https://doi.org/10.1016/j.febslet.2014.01.049

Suzuki, J., Kanemaru, K., Ishii, K., Ohkura, M., Okubo, Y., & Iino, M. (2014). Imaging intraorganellar Ca2+ at subcellular resolution using CEPIA. *Nat Commun*, *5*, 4153. https://doi.org/10.1038/ncomms5153

Szabó, Z., Héja, L., Szalay, G., Kékesi, O., Füredi, A., Szebényi, K., Dobolyi, Á., Orbán, T. I., Kolacsek, O., Tompa, T., Miskolczy, Z., Biczók, L., Rózsa, B., Sarkadi, B., & Kardos, J. (2017). Extensive astrocyte synchronization advances neuronal coupling in slow wave activity in vivo. *Scientific Reports*, *7*(1), 6018. https://doi.org/10.1038/s41598-017-06073-7

Takahashi, J. S. (2017). Transcriptional architecture of the mammalian circadian clock. *Nat Rev Genet*, *18*(3), 164-179. https://doi.org/10.1038/nrg.2016.150

Torrealba, N., Navarro-Marquez, M., Garrido, V., Pedrozo, Z., Romero, D., Eura, Y., Villalobos, E., Roa, J. C., Chiong, M., Kokame, K., & Lavandero, S. (2017). Herpud1 negatively regulates pathological cardiac hypertrophy by inducing IP3 receptor degradation. *Sci Rep*, *7*(1), 13402. https://doi.org/10.1038/s41598-017-13797-z

Tso, C. F., Simon, T., Greenlaw, A. C., Puri, T., Mieda, M., & Herzog, E. D. (2017). Astrocytes Regulate Daily Rhythms in the Suprachiasmatic Nucleus and Behavior. *Current Biology*, *27*(7), 1055-1061. https://doi.org/https://doi.org/10.1016/j.cub.2017.02.037

Tsunematsu, T., Sakata, S., Sanagi, T., Tanaka, K. F., & Matsui, K. (2021). Region-specific and state-dependent astrocyte Ca²⁺ dynamics during the sleep-wake cycle in mice. *The Journal of Neuroscience*, JN-RM-2912-2920. https://doi.org/10.1523/jneurosci.2912-20.2021

Verkhratsky, A., & Nedergaard, M. (2018). Physiology of Astroglia. *Physiol Rev*, *98*(1), 239-389. https://doi.org/10.1152/physrev.00042.2016

Vyazovskiy, V. V., Olcese, U., Lazimy, Y. M., Faraguna, U., Esser, S. K., Williams, J. C., Cirelli, C., & Tononi, G. (2009). Cortical firing and sleep homeostasis. *Neuron*, *63*(6), 865-878. https://doi.org/10.1016/j.neuron.2009.08.024

Wen, S., Ma, D., Zhao, M., Xie, L., Wu, Q., Gou, L., Zhu, C., Fan, Y., Wang, H., & Yan, J. (2020). Spatiotemporal single-cell analysis of gene expression in the mouse suprachiasmatic nucleus. *Nat Neurosci*, *23*(3), 456-467. https://doi.org/10.1038/s41593-020-0586-x

Wu, G., Anafi, R. C., Hughes, M. E., Kornacker, K., & Hogenesch, J. B. (2016). MetaCycle: an integrated R package to evaluate periodicity in large scale data. *Bioinformatics*, *32*(21), 3351-3353. https://doi.org/10.1093/bioinformatics/btw405

Wu, J., Liu, L., Matsuda, T., Zhao, Y., Rebane, A., Drobizhev, M., Chang, Y. F., Araki, S., Arai, Y., March, K., Hughes, T. E., Sagou, K., Miyata, T., Nagai, T., Li, W. H., & Campbell, R. E. (2013). Improved orange and red Ca^{2}± indicators and photophysical considerations for optogenetic applications. *ACS Chem Neurosci*, *4*(6), 963-972. https://doi.org/10.1021/cn400012b

Yagita, K., & Okamura, H. (2000). Forskolin induces circadian gene expression of rPer1, rPer2 and dbp in mammalian rat-1 fibroblasts. *FEBS Lett*, *465*(1), 79-82. https://doi.org/10.1016/s0014-5793(99)01724-x

Yang, R., & Su, Z. (2010). Analyzing circadian expression data by harmonic regression based on autoregressive spectral estimation. *Bioinformatics*, *26*(12), i168-174. https://doi.org/10.1093/bioinformatics/btq189

Yoo, S. H., Ko, C. H., Lowrey, P. L., Buhr, E. D., Song, E. J., Chang, S., Yoo, O. J., Yamazaki, S., Lee, C., & Takahashi, J. S. (2005). A noncanonical E-box enhancer drives mouse Period2 circadian oscillations in vivo. *Proc Natl Acad Sci U S A*, *102*(7), 2608-2613. https://doi.org/10.1073/pnas.0409763102

Yoshitane, H., Takao, T., Satomi, Y., Du, N. H., Okano, T., & Fukada, Y. (2009). Roles of CLOCK phosphorylation in suppression of E-box-dependent transcription. *Mol Cell Biol*, *29*(13), 3675-3686. https://doi.org/10.1128/mcb.01864-08

Zhang, R., Lahens, N. F., Ballance, H. I., Hughes, M. E., & Hogenesch, J. B. (2014). A circadian gene expression atlas in mammals: implications for biology and medicine. *Proc Natl Acad Sci U S A*, *111*(45), 16219-16224. https://doi.org/10.1073/pnas.1408886111

Zhang, X., Patel, S. P., McCarthy, J. J., Rabchevsky, A. G., Goldhamer, D. J., & Esser, K. A. (2011). A non-canonical E-box within the MyoD core enhancer is necessary for circadian expression in skeletal muscle. *Nucleic Acids Research*, *40*(8), 3419-3430. https://doi.org/10.1093/nar/gkr1297

Zhao, Y., Araki, S., Wu, J., Teramoto, T., Chang, Y. F., Nakano, M., Abdelfattah, A. S., Fujiwara, M., Ishihara, T., Nagai, T., & Campbell, R. E. (2011). An expanded palette of genetically encoded Ca^{2+} indicators. *Science*, *333*(6051), 1888-1891. https://doi.org/10.1126/science.1208592

Zou, Z., Ohta, T., Miura, F., & Oki, S. (2022). ChIP-Atlas 2021 update: a data-mining suite for exploring epigenomic landscapes by fully integrating ChIP-seq, ATAC-seq and Bisulfite-seq data. *Nucleic Acids Research*, *50*(W1), W175-W182. https://doi.org/10.1093/nar/gkac199

911 **Supplemental information**

912 **Table S1. Calcium ion homeostasis**

	MetaCycle		BioCycle		
Gene	p value	Amplitude	p value	Amplitude	Average TPM[a]
Herp	2.14E-09	11.66	0.00000001	11.35	71.13
Slc4a11	3.22E-09	1.48	0.00000100	1.50	6.68
Sord	3.60E-08	3.60	0.00002116	4.22	42.26
Kcnh1	5.50E-06	0.52	0.00000729	0.40	0.96
Anxa7	6.04E-06	4.44	0.00001444	4.23	102.07
Cx3cl1	3.13E-05	8.76	0.00019881	8.00	80.19
Pik3r1	5.21E-05	2.75	0.00126025	3.17	35.69
Hfe	0.000105052	2.94	0.00001600	2.95	32.10
Nr4a3	0.000106683	2.17	0.00064009	1.94	19.54
Spp1	0.000111664	31.47	0.00978121	41.58	168.53
Nppc	0.000162403	1.71	0.00017424	2.02	11.79
Sumo1	0.000462997	11.16	0.01687401	10.88	128.46
Tns2	0.000494944	1.01	0.00220900	1.21	13.15
Steap3	0.00050386	3.35	0.00494209	2.73	24.42
Capn1	0.000693268	2.57	0.00368449	2.49	48.74
Syt1	0.000707495	0.40	0.00015129	0.29	2.42
Ank	0.000906762	12.09	0.00077284	11.49	220.39
Casq2	0.001722008	0.67	0.00036864	0.64	5.78
Kcnj10	0.003437489	41.65	0.00088804	35.76	485.66
Adora1	0.005727835	6.56	0.00000009	7.08	63.08
P2ry1	0.006372537	1.77	0.00013225	1.99	19.40
Pcgf2	0.020637656	1.69	0.00090601	1.40	31.54
Dgat2	0.032505924	1.49	0.00055225	1.61	15.48

913 [a]Of all Time-merged values

914

915 **Table S2. *Herp* upstream 6kb region non-canonical E-Box**

E-box type	start position	end position	Upstream position	sequence	position
CANNTG	94380510	94380515	-5928	CATCTG	chr8:94380510-94380515
CANNTG	94381181	94381186	-5257	CAAGTG	chr8:94381181-94381186
CANNTG	94381199	94381204	-5239	CAGCTG	chr8:94381199-94381204
CANNTG	94381442	94381447	-4996	CAATTG	chr8:94381442-94381447
CANNTG	94381536	94381541	-4902	CAAGTG	chr8:94381536-94381541
CANNTG	94381563	94381568	-4875	CAGATG	chr8:94381563-94381568
CANNTG	94381689	94381694	-4749	CAAATG	chr8:94381689-94381694
CANNTG	94381721	94381726	-4717	CATCTG	chr8:94381721-94381726
CANNTG	94382162	94382167	-4276	CAATTG	chr8:94382162-94382167
CANNTG	94382173	94382178	-4265	CACCTG	chr8:94382173-94382178
CANNTG	94382368	94382373	-4070	CAGGTG	chr8:94382368-94382373
NC-CAGCTT	94382386	94382391	-4052	CAGCTT	chr8:94382386-94382391
CANNTG	94382714	94382719	-3724	CACCTG	chr8:94382714-94382719
CANNTG	94382896	94382901	-3542	CAGCTG	chr8:94382896-94382901
CANNTG	94383317	94383322	-3121	CATATG	chr8:94383317-94383322
CANNTG	94383445	94383450	-2993	CAGATG	chr8:94383445-94383450
CANNTG	94384166	94384171	-2272	CAAGTG	chr8:94384166-94384171
CANNTG	94384284	94384289	-2154	CATTTG	chr8:94384284-94384289
NC-CACGTT	94384539	94384544	-1899	CACGTT	chr8:94384539-94384544
CANNTG	94384874	94384879	-1564	CAAATG	chr8:94384874-94384879
CANNTG	94384902	94384907	-1536	CACATG	chr8:94384902-94384907
CANNTG	94385063	94385068	-1375	CAGCTG	chr8:94385063-94385068
CANNTG	94385102	94385107	-1336	CAAATG	chr8:94385102-94385107
CANNTG	94385331	94385336	-1107	CAGGTG	chr8:94385331-94385336
CANNTG	94385353	94385358	-1085	CATGTG	chr8:94385353-94385358
NC-CAGCTT	94385511	94385516	-927	CAGCTT	chr8:94385511-94385516
CANNTG	94385809	94385814	-629	CAGATG	chr8:94385809-94385814
CANNTG	94385910	94385915	-528	CACTTG	chr8:94385910-94385915
NC-CACGTT	94386384	94386389	-54	CACGTT	chr8:94386384-94386389

916

917

918 **Table S3: Table of primers used in quantitative RT-PCR**

Primers	SOURCE
Bmal1 F: CAC CTA ATT CTC AGG GCA G	Marcrogen
Bmal1 R: CAC CTA ATT CTC AGG GCA G AGA CTC GGA GAC AAA GAG G	Marcrogen
Nr1d1(Rev-erb α) F: AAT GTT CTG CTG GCA TGT C	Marcrogen
Nr1d1(Rev-erb α) R: GAA GTC TTC CCA GAT CTC CT	Marcrogen
Hprt F: GATTAGCGATGATGAACCAGGT	Marcrogen
Hprt R: CCTCCCATCTCCTTCATGACA	Marcrogen
Herp F: GGT GGA GGA AGA TGA TGA GAT AAA	Marcrogen
Herp R: CTC AGC GAG GAG TAG AAG TAA AG	Marcrogen

919

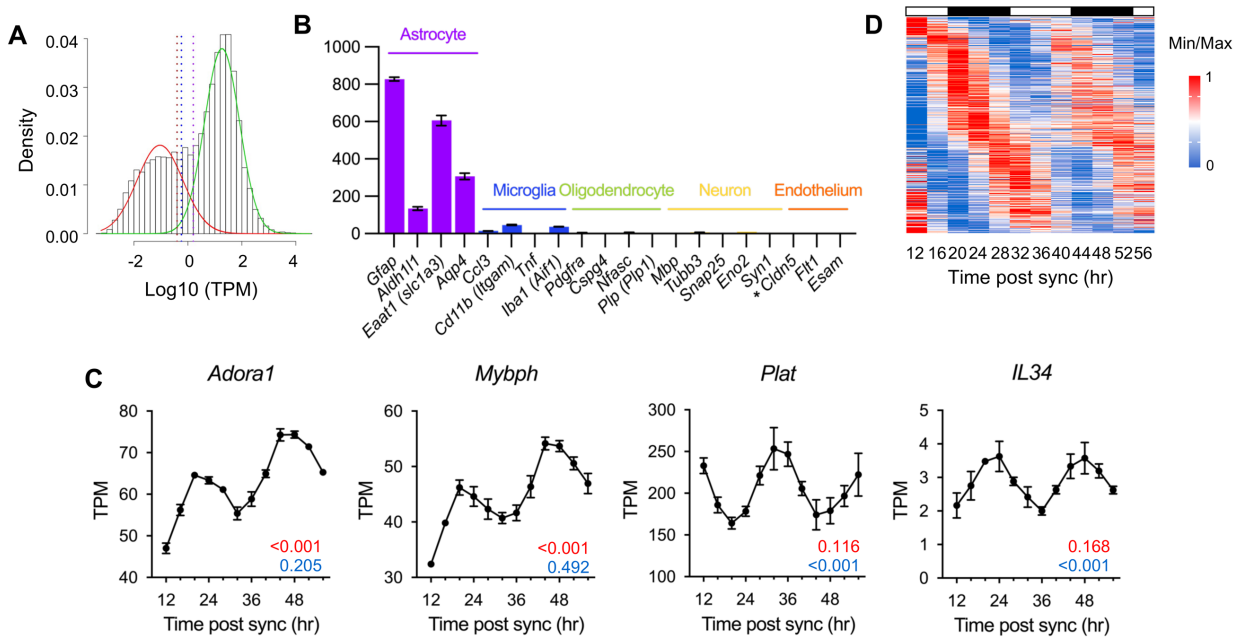

Figure 1-figure supplement 1. Identification of circadian rhythmic transcripts in mouse cultured astrocytes (A) Histogram showing the distribution of mean expression levels of transcripts. Transcripts with low (red) and high (green) expression were identified using a Gaussian mixture model. Dashed vertical lines represent cut-off points for highly expressed transcripts: maroon line (99.5%, TPM 0.40), blue line (99.0%, TPM 0.57), and purple line (95.0%, TPM 1.59). (B) Time-averaged expression levels of marker genes for astrocytes, microglia, oligodendrocytes, neurons, and endothelial cells in astrocyte cultures. Values are mean TPM ± S.E.M (n = 2); *, not detected. (C) Expression profiles of *Plat*, *Il34*, *Adora1*, and *Mybph* in SS-synchronized cultured astrocytes from RNA-seq data. The q-values for BioCycle (red) and MetaCycle (blue) are shown in the bottom right corner. (D) Heatmap of 412 candidate genes from RNA-seq data, ordered by MetaCycle phase. Expression levels were normalized using Min-Max normalization.

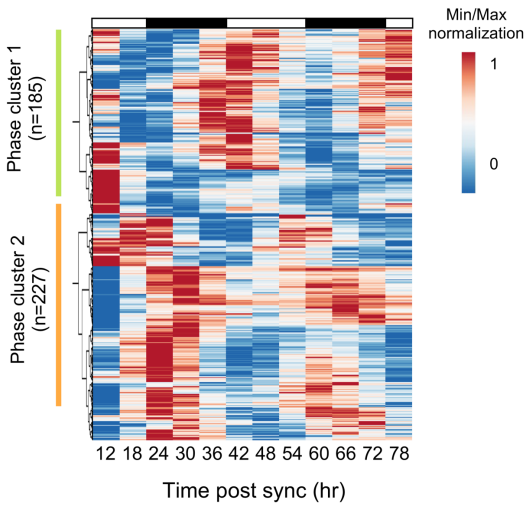

934

935 **Figure 1-figure supplement 2. Cluster analysis of circadian rhythmic transcripts.** Cluster analysis of
936 412 candidate genes was performed using ClustVis (https://biit.cs.ut.ee/clustvis/)(Metsalu & Vilo, 2015).
937 Expression levels were normalized using Min-Max normalization. Green bar indicates Cluster 1; orange
938 bar indicates Cluster 2.

939

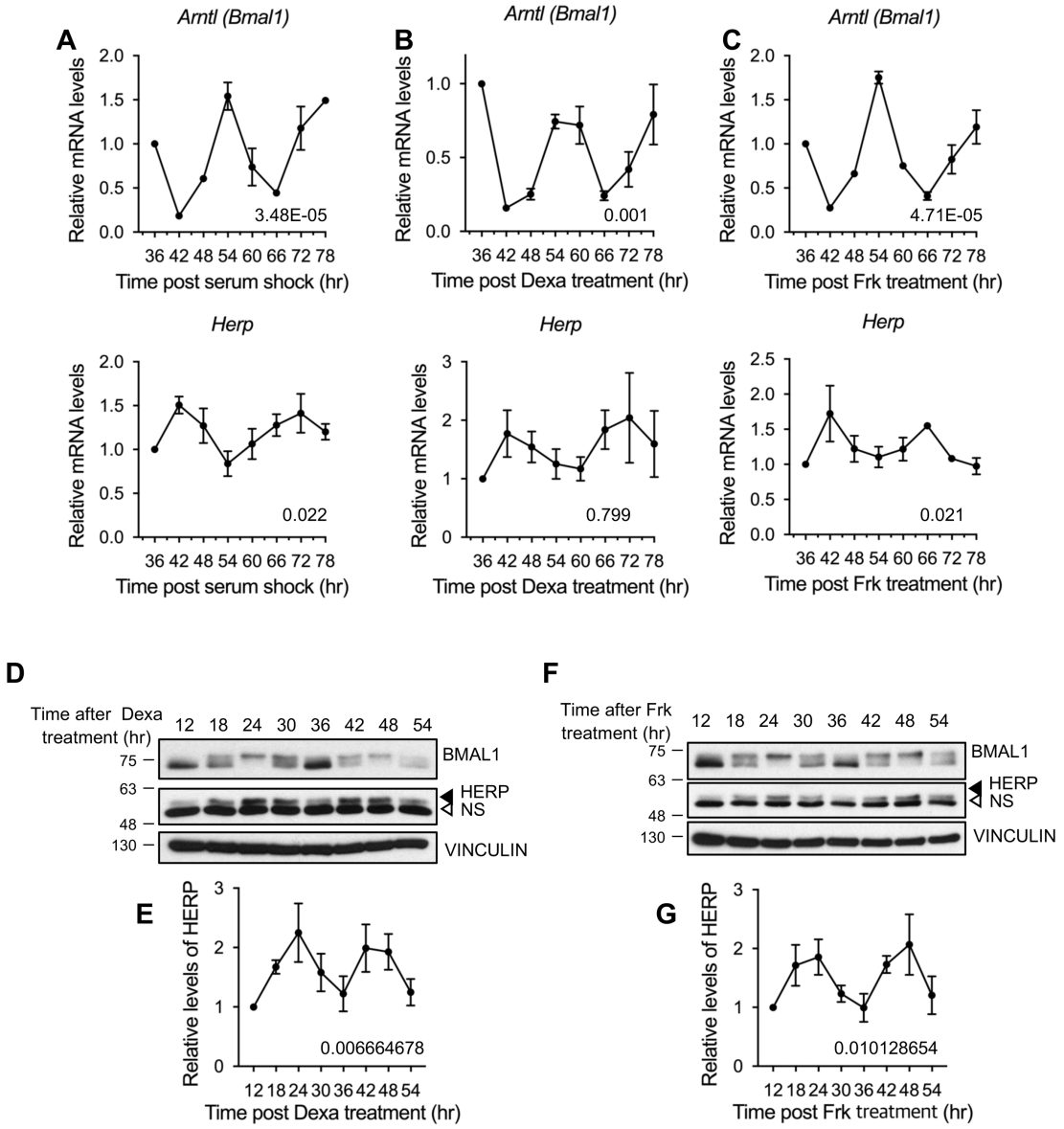

Figure 2-figure supplement 1. Herp is rhythmically expressed in mouse cultured astrocytes synchronized by forskolin or dexamethasone. Astrocytes were synchronized using 50% horse serum (A), 100 nM dexamethasone (B, D-E), or 10 μM forskolin (C, F-G), and harvested at the indicated times. (A-C) Real-time qRT-PCR was performed to examine mRNA levels of the indicated genes (D-G) Western blot analysis for BMAL1 and HERP was conducted, with VINCULIN as a loading control. HERP/VINCULIN values at different times were normalized to those at 12hrs post-shock (set to 1). (D, F) Representative Western blot images from three independent experiments. (E, G) Densitometric quantification of Western blots. Rhythmicity was analyzed using MetaCycle. Meta2d *p* values are indicated by insets in graphs. Values are mean ± SEM (n = 3); *p*-values are indicated in the graph insets.

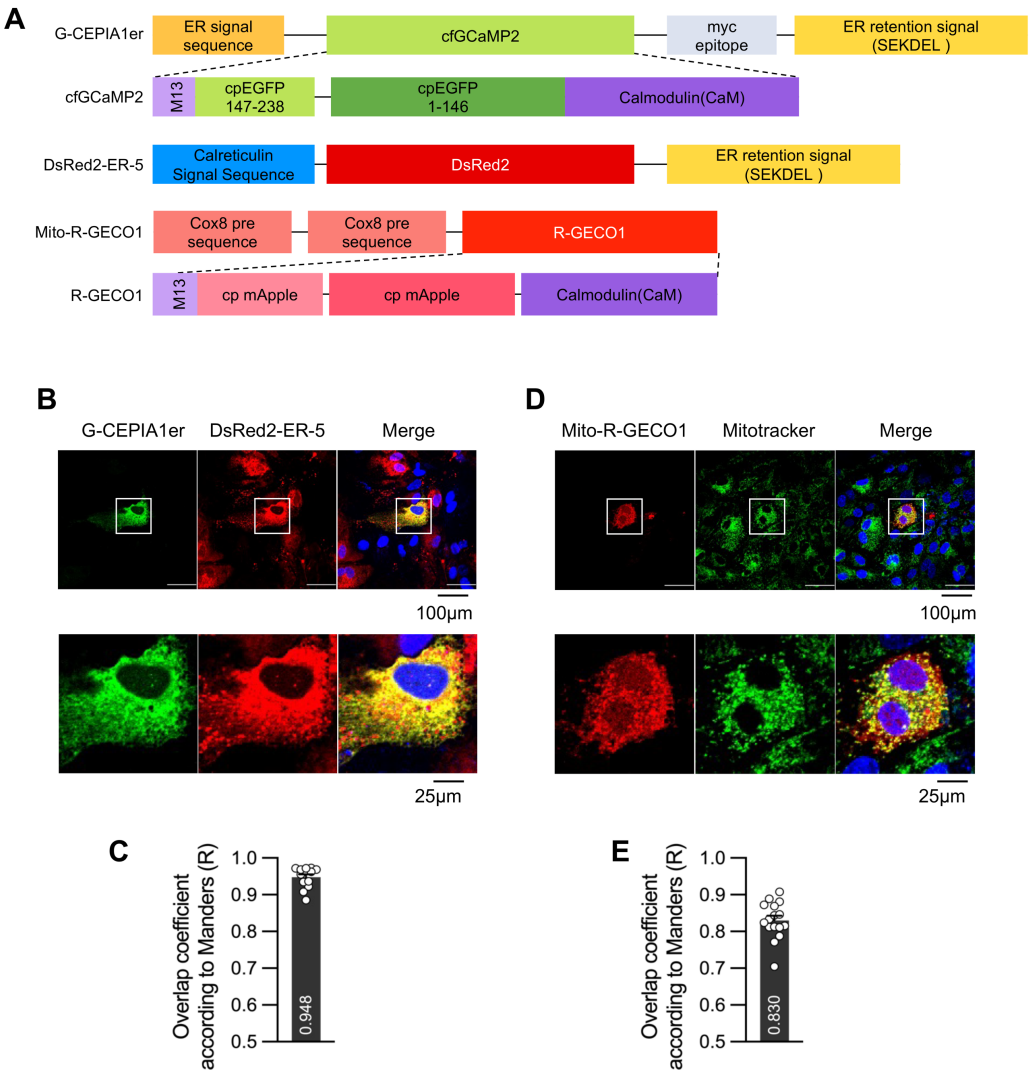

951

952 **Figure 3-figure supplement 1. Co-localization of organelle-specific Ca^{2+} sensors with organelle**
953 **markers.** (A) Schematic diagram showing organelle-specific Ca^{2+} sensors and DsRed2-ER-5. Astrocytes
954 were transfected with Ca^{2+} sensors specific for G-CEPIA1er (B, C) or mito-R-GECO1 (D, E). (B, C) G-
955 CEPIA1er was co-transfected with DsRed2-ER-5 containing calreticulin signal sequence. Live-cell
956 imaging was performed 48hrs post transfection. (D, E) Mito-R-GECO1 was transfected, and live-cell
957 imaging was performed 48hrs post transfection. Before imaging, 200nM Mitotracker was applied for 30
958 minutes to stain the mitochondria. (C, E) The overlap coefficient (Manders' R value) was calculated from
959 the images. (B, C) n = 13; (D, E) n = 16

960

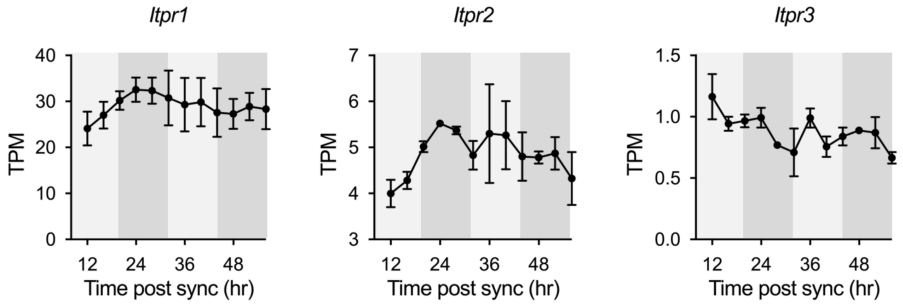

Figure 3-figure supplement 2. Expression profiles of Itpr1, Itpr2 and Itpr3 in cultured astrocytes from RNA-seq data. White and gray backgrounds represent subjective day and subjective night, respectively.

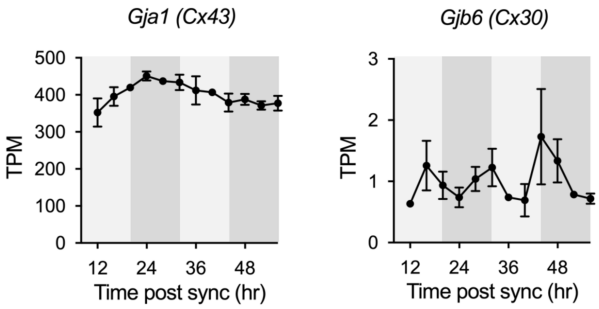

967

968 **Figure 6-figure supplement 1. Expression profiles of Cx43 and Cx30 in cultured astrocytes from**
969 **RNA-seq data.** White and gray backgrounds represent subjective day and subjective night, respectively.

970

SI References

Metsalu, T., & Vilo, J. (2015). ClustVis: a web tool for visualizing clustering of multivariate data using Principal Component Analysis and heatmap. *Nucleic Acids Res*, *43*(W1), W566-570. https://doi.org/10.1093/nar/gkv468